J. Fluid Mech. (1995), *vol.* 297, *pp.* 153–191

Fluid flow in loops driven by freshwater and heat fluxes

By W. K. DEWAR[1] AND R. X. HUANG[2]

[1]Department of Oceanography, Supercomputer Computations Research Institute and the Geophysical Fluid Dynamics Institute, The Florida State University, Tallahassee, FL 32306-3048, USA

[2]Department of Physical Oceanography, The Woods Hole Oceanographic Institution, Woods Hole, MA 02543, USA

(Received 25 October 1994 and in revised form 30 March 1995)

Thermohaline convection in a salt water loop is discussed. Fluid temperature is affected by relaxation on the loop surface and fluid salinity by a freshwater flux through the loop surface. In addition, other boundary conditions on salinity, such as the equivalent virtual salt flux or salinity relaxation condition, are examined and the dynamic role of diffusion in thermohaline convection is analysed.

Both analytical and numerical analyses indicate that the system behaviour depends sensitively on the nature of the salinity boundary condition. For the saline-only loop model, analysis indicates that perturbations are advected by the mean flow, and flow stability is independent of the strength of the boundary forcing. In the full thermohaline loop problem, the virtual salt flux formulation accurately mirrors the freshwater flux results when the system is in the thermal mode. However, these formulations can differ substantially when the system is in the haline mode, especially in the strongly forced, weakly diffusive limit.

For both types of loop configuration, salinity profiles governed by freshwater flux have scales determined by the internal parameters, while virtual salt flux profiles necessarily reflect the lengthscales of applied boundary conditions. Negative salinities can also appear under virtual salt flux owing to the inaccuracies inherent in the approximation, while freshwater flux ensures positive-definite salinity values.

Our analysis supports the use of the physically more accurate freshwater flux boundary conditions when simulating thermohaline circulation.

1. Introduction

A problem of considerable significance in fluid mechanics is that of convection. Numerous past convection studies have examined fluids whose density is set by heat; a far smaller number have considered fluids with dissolved solutes, where density can be affected by the addition or removal of freshwater. Associated with this is a considerable distinction in the interactions of these two fluid types with their environments.

Here we use the classical loop oscillator paradigm to analyse convection in the latter type of fluid. First, the impact of freshwater flux on convection in fluids with solutes is computed and compared to the behaviour found using approximations of such forcing. (The latter are widely used in climate models.) Secondly, convection in a fluid sensitive to both heat and solute concentration is calculated. Both of these areas are suggested by, and have implications for, climate modelling.

1.1. *Background*

Loop models have been used extensively in the study of thermal convection. Early works include those of Keller (1966), Welander (1967) and Malkus (1972). More recently, such models have received considerable attention in the engineering literature (see Wang & Bau 1992 for a recent review). In the classical studies, the fluid was heated from below and cooled from above by means of relaxation conditions on temperature. Some recent oceanic thermohaline models have exhibited decadal scale variability, the dynamics of which have been linked to the mechanics in these models (e.g. Welander 1967 and, more recently, Walin 1985). The full density of seawater, however, is set jointly by temperature (T) and salinity (S), and loop oscillator studies in an oceanic context, in which both T and S were subject to relaxation, have been conducted by Welander (1986). Winton & Sarachik (1993) examined a variant of the Welander model (T was fixed in their calculations) in order to diagnose the dynamics of the salt oscillations found in their two- and three-dimensional general circulation model results.

The motivation for the latter studies of the so-called thermohaline circulation come from satellite radiation measurements, which suggest that the oceans and atmosphere play comparable roles in setting the climate of the Earth (Trenberth & Solomon 1994). The models which have been brought to bear on the climate problem range from very complex coupled ocean–atmosphere numerical simulations to simple process-oriented analytical models. An example of the latter, which has had tremendous impact on the field, is the classical box model of Stommel (1961). In this deceptively simple calculation, boxes connected by pipes exchanged fluid at rates determined by their relative densities. These densities in turn were set by the competing effects of heat and salt, and it was demonstrated that the differing properties of these quantities led to more than one possible circulation pattern. The potential for the oceanic overturning cell to exist in more than one configuration is clearly of considerable significance to the Earth's climate in general, as well as to our capacity to assess the climatic impact of human activity.

Since the appearance of this seminal work, box models have been used to examine several aspects of the oceanic thermohaline circulation and have also proven useful in diagnosing the climate mechanics of numerical general circulation models (GCMs). In spite of their elegance, it must, however, be admitted that box models do not readily allow an examination of several processes which are probably essential to GCM performance and to the real climate. This serves as partial motivation for our efforts here to examine thermohaline convection through an analysis of a very simple loop oscillator. This model represents a level of complexity (and hopefully realism) beyond box models, while retaining sufficient simplicity so as to allow extensive study. We discuss here rather simple model geometries and forcing fields, thus yielding analytical and numerical tractability. Cases with more complicated geometry and forcing fields can easily be studied numerically.

1.2. *Salinity boundary conditions*

Early numerical investigations of climate generally modelled the exchanges of heat and salinity at the air–sea interface by means of identical relaxation laws (frequently referred to as 'Haney' relaxation). This occurred even though Stommel (1961) suggested that significant aspects of climate behaviour depended on the differences in their surface exchange processes. The modern era of climate modelling was opened by Bryan (1986), who examined a primitive-equation general circulation model subject to

so-called 'mixed' boundary conditions (consisting of a relaxation law on temperature and a specification of salinity flux). He demonstrated the existence of multiple equilibria in such models, the nature of which were consistent with those originally predicted by Stommel (1961). Since this exciting result, many numerical studies involving mixed boundary conditions have been conducted (Marotzke & Willebrand 1991; Weaver & Sarachik 1991; England 1993), and much attention has been given to the different sorts of steady states resident therein, as well as to the existence of oscillatory solutions. Many of these GCM studies have been at least partially understood through the use of box models (Thual & McWilliams 1992; Marotzke 1994).

Among other things, these studies show that the distinction between heat and salinity surface boundary conditions is central to the existence of multiple thermohaline equilibria. It is nonetheless true that 'mixed' boundary conditions, as they are routinely implemented, distort the physics of the surface exchange processes relevant to salinity. The distortion comes because the boundary conditions specify the flux of salinity through the sea surface, while in the real ocean salinity is affected by means of the freshwater flux due to evaporation and precipitation. Climate models are in practice very sensitive to small variations in their structure. It is thus not clear to what extent the behaviour present in GCMs represents the distorted physics inherent in such 'virtual salt flux' (VSF) boundary conditions. In a related vein, our understanding of the circulation generated by evaporation and precipitation alone in a stratified ocean far lags our knowledge of that of due to wind and heating, the latter two having been the subject of decades of work.

Huang (1993) emphasized the proper boundary condition on salinity, pointing out that net salt flux vanishes at the surface, and that evaporation and precipitation affect the system through the continuity equation. He presented numerical solutions for the three-dimensional structure of this 'haline' circulation, emphasizing the importance of applying his salinity boundary condition (which he termed the 'natural boundary condition' (NBC)). Huang further demonstrated that a system forced by freshwater flux alone could oscillate (a concept first proposed by Broecker *et al.* 1990). In a subsequent study, the haline circulation and oscillations were examined over a broad parameter range (Huang & Chou 1994).

1.3. *This paper*

The main objective of this paper is to contribute to our conceptual understanding of convection in thermohaline systems by means of a relevant analysis of a loop model. The particular points we choose to emphasize are of relevance to climate modelling, which has a rich tradition in the realm of analytical process models. Density in the loop is affected by both temperature and salinity and it is in the implementation of their relevant boundary conditions that the main differences between the present work and past loop oscillator studies are found. Relaxation boundary conditions are employed for heat, as is standard, but both the less widely used NBC and more popular VSF boundary conditions on salinity are studied. The main issues we address involve illustrating the unique convective behaviour of a stratified fluid subject to the NBC and clarifying the effects of diffusion on the thermohaline circulation.

Accordingly, we find the impact of the NBC on the structure of a convecting loop to be profound and to introduce surprising and counter-intuitive tendencies. Further, the comparison between these results and those found using VSF conditions suggests limitations on the use of the latter. A number of interesting comparisons are also to be made between the original Stommel model and the present study. For example,

parameter combinations arise which are analogous to *ad hoc* processes in the Stommel model. We also find that our model exhibits a self-sustaining saline mode oscillation. The above results are supported by both analytical and numerical computation.

The model equations are described in the next section and a description of the numerical methods is given. Analytical and numerical solutions of the salt-only loop are discussed in §3, an analysis of the thermohaline loop appears in §4 and the paper closes with a discussion of the results and some conclusions.

2. Equations of motion and computational methods

Consider a closed circular loop filled with a saline fluid and employ a radial coordinate system with azimuthal angle $\theta = 0$ at the loop bottom (see figure 1). Gravity acts in the downward direction. The radius of the closed tube is r_0 and the inner radius of the loop is R_0. We assume $r_0/R_0 \ll 1$ and therefore that many of the fluid's properties are well mixed across the tube.

Fluid density is assumed to be sensitive to both temperature and salinity. Heat is exchanged through the skin of the tube according to the flux law:

$$A_T T_r[R_0+2r_0] = -\Gamma(T-\bar{T}), \tag{2.1a}$$

where Γ is a relaxation timescale, T fluid temperature, A_T heat diffusivity and $\bar{T}$ a reference temperature profile. The tube and the environment also exchange freshwater according to

$$u[R_0+2r_0] = \bar{e}, \tag{2.1b}$$

where u is the fluid radial velocity and $\bar{e}$ is a reference freshwater flux profile. (Note that we are glossing over latent heat flux effects here; more about this shortly.)

2.1. *Continuity*

The $\bar{e}$ profile affects the salinity distribution through the continuity equation by the addition of pure water to an otherwise salty fluid. To see this, the continuity equation

$$\frac{\partial}{\partial r}(ru)+\frac{\partial}{\partial \theta}V = 0, \tag{2.2}$$

where u is the radial velocity and V the azimuthal velocity, is integrated radially across the tube to yield

$$V_\theta = -\frac{R_0}{2r_0}\bar{e}+O\left(\frac{r_0}{R_0}\right). \tag{2.3}$$

For definiteness, we choose $\bar{e} = -E\cos(\theta-\theta_p)$, where θ_p defines the orientation of the freshwater flux field. Thus

$$\frac{V}{R_0} = \omega = \Omega+\frac{E}{2r_0}\sin(\theta-\theta_p), \tag{2.4}$$

where ω denotes angular fluid velocity and Ω is a function of time only. Thus we see that the total azimuthal velocity in this model consists of a non-divergent variable part and a spatially fixed, but divergent, part which exists to satisfy the evaporation–precipitation boundary condition. This latter contribution to the flow field is due entirely to the freshwater flux boundary condition, and has no counterpart in a flow subject to virtual salt flux.

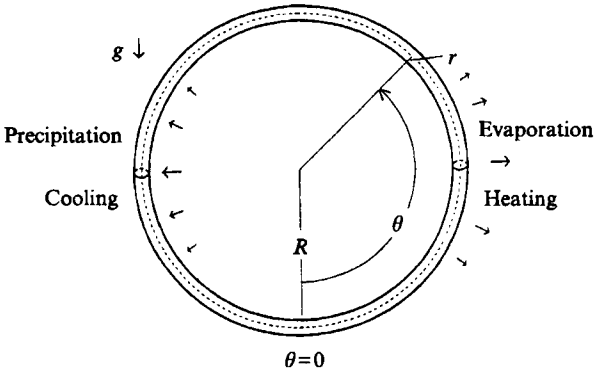

FIGURE 1. Loop schematic. We consider a loop filled with salty water. Freshwater and heat are exchanged through the loop surface. Gravity acts in the downward direction and the fluid generates azimuthal velocity in response to density variations. The forcing fields can have arbitrary orientation: those shown employ (*a*) $\theta_p = 0$ and (*b*) $\theta_p = -\pi/2$, $\theta_T = \pi/2$.

2.2. *Salt conservation*

The equation of salt conservation is

$$S_t + uS_r + \frac{V}{r}S_\theta = \frac{A_S}{r}\frac{\partial}{\partial r}r\frac{\partial}{\partial r}S + \frac{1}{r^2}A_S S_{\theta\theta}, \tag{2.5}$$

where A_S is a coefficient of salt diffusion. Upon an integration in r and use of the natural boundary conditions $[A_S S_r - uS] = 0$ (Huang 1993) at the loop boundaries, we obtain

$$S_t + (\omega S)_\theta = \frac{A_S}{R_0^2}S_{\theta\theta}. \tag{2.6a}$$

Note that (2.6*a*) implies

$$\frac{\partial}{\partial t}\int_0^{2\pi} S\,\mathrm{d}\theta = 0,$$

so that the total salt in the loop remains fixed. Such a constraint is the immediate result of the natural boundary conditions. For comparison, the salt conservation equations subject to virtual salt flux and relaxation boundary conditions are

$$S_t + (\Omega S)_\theta = \frac{-E}{2r_0}\bar{S}\cos\theta + \frac{A_S}{R_0^2}S_{\theta\theta}, \tag{2.6b}$$

$$S_t + (\Omega S)_\theta = \frac{\Gamma_S}{2r_0}(S^* - S) + \frac{A_S}{R_0^2}S_{\theta\theta}, \tag{2.6c}$$

where Γ_S is a salinity relaxation coefficient, $\bar{S}$ an average salinity and S^* a specified reference salinity (traditionally chosen to be the observed salinity). Note that the net salt in the problem is guaranteed to be a constant if (2.6*a*) is used. If the net freshwater flux vanishes, (2.6*b*) also conserves net salt. No such guarantee exists for (2.6*c*).

2.3. *Temperature conservation*

Comparable manipulations of the heat equation yield

$$T_t + \omega T_\theta = -\Gamma(T - \bar{T}) + \frac{A_T}{R_0^2}T_{\theta\theta}, \tag{2.7}$$

where A_T is a coefficient of thermal diffusion and we have assumed the temperature of rainfall is identical to the local fluid temperature of the loop (thereby removing heat fluxes associated with precipitation). The form of (2.7) is such that both T and $\bar{T}$ can be measured relative to some absolute temperature, provided that the same reference is used for both. We adopt this convention (thus T and $\bar{T}$ can be both positive and negative) and for definiteness, will use $\bar{T} = \bar{T}_0 \cos(\theta - \theta_T)$, where θ_T defines the orientation of the reference temperature profile and, like θ_p, is arbitrary.

2.4. *Momentum equation*

Dynamical constraints on Ω can be obtained from the azimuthal momentum equation:

$$V_t + uV_r + \frac{VV_\theta}{r} + \frac{uV}{r} = -\frac{1}{r}p_\theta + \frac{\sigma}{r}\frac{\partial}{\partial r}r\frac{\partial}{\partial r}V + \frac{\sigma}{r^2}V_{\theta\theta} - g\rho' \sin\theta, \tag{2.8}$$

where σ is viscosity and other notation is standard. This equation is modified by a multiplication by r^2, a radial integration across the tube and an azimuthal averaging to yield

$$\Omega_t = -\nu\Omega - g\langle \rho' \sin\theta \rangle / R_0, \tag{2.9}$$

where $\langle \cdot \rangle = (1/2\pi)\int_0^{2\pi} \cdot \, d\theta$ denotes an averaging operator. To obtain (2.9), we have assumed that precipitation possesses an azimuthal angular momentum of Ω (so that momentum fluxes due to rainfall vanish) and that frictional interactions with the tube walls can be written as a drag, i.e.

$$\sigma V_r = -\nu V / R_0. \tag{2.10}$$

The equation set (2.6*a*, *b* or *c*) and (2.9) are closed by the inclusion of the linear equation of state:

$$\rho' = \beta S - \alpha T. \tag{2.11}$$

2.5. *Non-dimensionalization*

Equation (2.6) guarantees that the loop contains a fixed amount of salt, from which we obtain the salinity scale $\bar{S} = \langle S \rangle$. This, in turn, implies a reduced gravity magnitude of $g\beta\bar{S}$, which in a loop of radius R_0 results in an overturning timescale of $[R_0/g\beta\bar{S}]^{1/2} = \tau_0$. Scaling both ω and time by τ_0, salinity by $\bar{S}$ and temperature by $\bar{T}_0$ eventually leads to the non-dimensional set

$$S_t + [(\Omega + \lambda \sin(\theta - \theta_p))\, S]_\theta = \kappa_S S_{\theta\theta}, \tag{2.12a}$$

$$T_t + (\Omega + \lambda \sin(\theta - \theta_p))\, T_\theta = -\gamma(T - \Delta \cos(\theta - \theta_T)) + \kappa_T T_{\theta\theta}, \tag{2.12b}$$

$$\Omega_t + \alpha\Omega = -\langle S \sin\theta \rangle + \frac{1}{R}\langle T \sin\theta \rangle, \tag{2.12c}$$

where

$$\lambda = \frac{E\tau_0}{2r_0}, \quad \kappa_S = A_S\frac{\tau_0}{R_0^2}, \quad \kappa_T = \frac{A_T\tau_0}{R_0^2}, \quad \alpha = \nu\tau_0, \quad \gamma = \Gamma\tau_0, \quad R = \frac{\beta\bar{S}}{\alpha\bar{T}_0}.$$

Identifying τ_0 as a 'flushing' timescale, λ represents the ratio of τ_0 to a tube filling time based on precipitation, α the ratio of τ_0 to viscous decay time, κ_S and κ_T the ratio of τ_0 to diffusion times for salt and heat, respectively, and γ the ratio of τ_0 to the temperature relaxation timescale. The density ratio parameter R measures the relative

importance of salt to heat in determining fluid density; an analogous parameter 'R' appears in Stommel (1961). Finally, the factor of Δ in front of the thermal relaxation profile in (2.12*b*) takes the value $1/2$ in order to ensure that the total temperature range corresponds to $\bar{T}_0$.

Six non-dimensional parameters α, κ_S, κ_T, λ, γ, and R appear in the above equations. Since we are in the early stage of learning about the dynamics of the loop oscillator subject to NBC, we choose to examine the weakly forced, weakly viscous limit, i.e. $\alpha \approx \lambda \ll O(1)$. Such a parameter ordering is chosen for convenience, and there is clearly some ambiguity in the selection of parameter values, in recognition of the idealized nature of our model and our interest in the climate. While the above regime seems a reasonable one to study, and certainly pertinent to climate issues, it is almost certainly not the only one. However, a more comprehensive exploration of the parameter space is left for further study.

The parameters κ_T and κ_S will take a wider range of values, from $O(1)$ to values much less than $O(\alpha, \lambda)$. In terms of our climate motivation, the above (particularly the weak mixing limit) represents a sensible regime, and corresponds to water vapour fluxes that are small compared to oceanic mass fluxes. The latter is consistent with the argument put forward in Broecker, Peteet & Rind (1985) which emphasizes the climatic significance of $O(1$ Sv) atmospheric water vapour fluxes (compared to a thermohaline overturning cell of $O(20$ Sv)). In contrast, boundary layer meteorologists emphasize the strong negative feedbacks between the atmosphere and the ocean which tend to remove sea surface temperature anomalies. This translates in numerical GCMs to fairly short relaxation timescales and hence a considerable boundary condition control of temperature. This will be reflected in our loop model studies by choosing a larger value for γ than for α, λ, κ_S or κ_T. Finally, with $\alpha \approx 2 \times 10^{-4}$ °C^{-1}, $\beta \approx 8 \times 10^{-4}$ (practical salinity units)$^{-1}$, $\bar{T}_0 \approx 30$ °C and $\bar{S} \approx 35$ practical salinity units, $R \approx 4$.

2.6. *Numerical methods*

The focus of the next two sections will be the solutions of (2.12), and both analytical and numerical approaches will be discussed. We therefore briefly indicate our numerical methods here. Of principal importance in their selection is the fact that the temperature and salinity fields are periodic, which leads naturally to the use of spectral methods. Another advantage of this approach is that the temperature and salinity torques appearing in the momentum equation occur naturally as the lowest mode of the temperature and salinity Fourier expansion. Most of the numerical results presented in the next section used 64 azimuthal modes; tests with 128 and 256 modes indicated that our main results are not sensitive to resolution. A fourth-order Runge–Kutta time-stepping procedure was used to compute the evolution of the spectral coefficients.

3. A salt-only model

We first consider a special case of (2.12), corresponding to a loop filled with salty water forced only by a freshwater flux. The equations governing this system are obtained from the above by ignoring T. This corresponds to $\gamma = 0$, which under normal evolution will ultimately yield $T = 0$. Thus (2.12*c*) becomes

$$\Omega_t = -\alpha\Omega - \langle S \sin\theta \rangle.$$

It is perhaps not surprising that the nature of the stationary solutions depends critically on the relative importance of the parameters α, λ and κ (here $\kappa = \kappa_S$ for

convenience). When $\kappa \equiv 0$, it is straightforward to find the steady solution of (2.12); i.e. for arbitrary α and λ

$$S = \frac{[1-(\lambda/\Omega)^2]^{1/2}}{1+(\lambda/\Omega)\sin\theta},$$

where

$$\Omega = \pm\left(\frac{\lambda}{\alpha(2-\alpha\lambda)}\right)^{1/2}$$

is the mean angular velocity.

It is, however, much more interesting to consider non-zero κ because diffusion exists in reality and is also necessary for numerical stability. In addition, we will show that small, but non-zero, κ gives rise to very interesting limit-cycle behaviour.

We have also set $\theta_p = 0$, yielding a loop which is evaporated from above and precipitated on from below. In some sense, this situation is the analogue for salty fluids of the classical thermal convection problem. As stated above, we consider here small α and λ, and for analytical convenience will also assume $\alpha \sim \lambda \ll 1$. When κ is non-zero, the solutions for Ω and S can be simply obtained by employing a perturbation approach which makes use of these parametric restrictions. Indeed, a convenient classification of this form of (2.12) is found if we consider κ larger than, comparable to and smaller than α and λ, respectively. We shall now describe this classification.

3.1. *The diffusive limit* (α, $\lambda \ll \kappa \leqslant O(1)$)

Neglecting time derivatives in (2.12*a*) and expanding in λ yields at lowest order

$$\Omega_0 S_{0\theta} = \kappa S_{0\theta\theta}, \tag{3.1}$$

where the subscript denotes the order of the expansion. The solution of (3.1) subject to periodicity and the normalization condition is

$$S_0 = 1. \tag{3.2}$$

Note that this solution is consistent with the steady lowest-order form of (2.12*c*).

The next order in λ yields

$$\Omega_0 S_{1\theta} = -\cos\theta + \kappa S_{1\theta\theta}. \tag{3.3}$$

The solution of this equation for S_1, subject to periodicity and normalization, is simply

$$S_1 = -\frac{\kappa}{\Omega_0^2+\kappa^2}\left(\cos\theta + \frac{\Omega_0}{\kappa}\sin\theta\right). \tag{3.4}$$

Inserting (3.4) in (2.12*c*) yields three solutions for Ω_0, i.e.

$$\Omega_0 = \pm\left(\frac{\lambda}{2\alpha} - \kappa^2\right)^{1/2}, \quad \Omega_0 = 0. \tag{3.5}$$

Thus for $\kappa^2 > \lambda/2\alpha$ the only physically acceptable solution is that the ring is at rest, i.e. $\Omega = 0$. The salinity profile

$$S = 1 - \frac{\lambda}{\kappa}\cos\theta$$

is simply left–right symmetric with respect to the forcing and with a maximum at

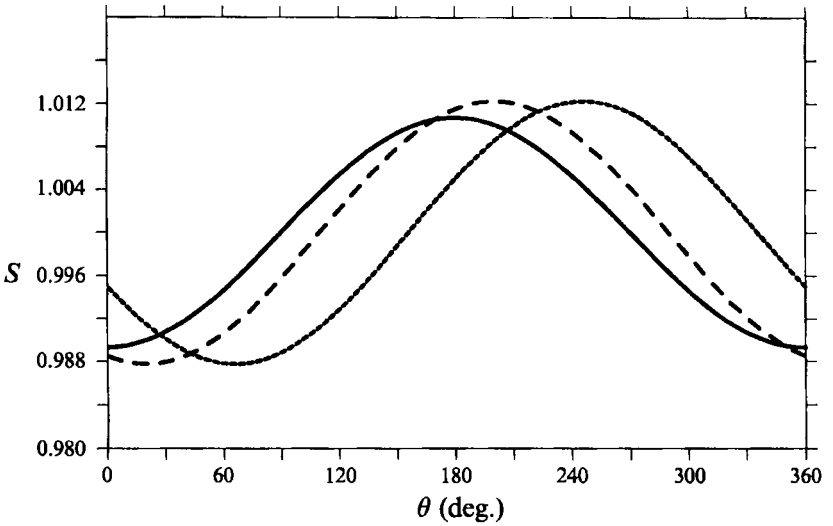

FIGURE 2. Diffusively dominated solutions for $\alpha = 0.0055$, $\lambda = 0.015$ and $\kappa = 1.4$ (solid line), $\kappa = 1.15$ (long dashed line) and $\kappa = 0.5$ (short dashed line). The associated Ω-values were determined numerically to be 0, 0.2 and 1.0 respectively.

$\theta = \pi$, as indicated by the solid curve in figure 2. The secondary circulations associated with the freshwater flux profile (represented in (2.12*a*) by the $\lambda \sin\theta$ term) advect the mass from source to sink. The salinity variations of $O(\lambda)$ are set up by a balance between the mass flux convergence/divergence and salt diffusion.

The situation changes for κ smaller than the critical parameter value $\kappa_c = (\lambda/2\alpha)^{1/2}$; namely, the possibility of a non-zero circulation arises in which the salinity maximum is located at

$$\theta_0 = \pi \pm \tan^{-1}\left(\frac{\lambda}{2\alpha\kappa^2} - 1\right)^{1/2}. \tag{3.6}$$

The nature of the solution in (3.6) is that, as κ decreases, the salinity maximum moves away from $\theta = \pi$ toward either $\theta = \frac{3}{2}\pi$ or $\frac{1}{2}\pi$, depending on whether Ω_0 is positive or negative, respectively.

It is a simple matter to demonstrate that the stagnant solution is stable for $\kappa > \kappa_c$ (some of the mathematical steps are included in the next section). For $\kappa < \kappa_c$, the solution with circulation ($\Omega_0 \neq 0$) is stable, but the solution with $\Omega_0 = 0$ is unstable. Such behaviour is identified in dynamical systems theory as a pitchfork bifurcation (see figure 3).

We have tested the validity of these solutions using the above-mentioned numerical code; salinity profiles appear in figure 2. The parameter values used here were $\alpha = 0.0055$ and $\lambda = 0.015$, yielding a critical value for κ of $\kappa_c \approx 1.25$. A κ-value of 1.4 was used to produce the solid curve and a value of 1.15 was used to produce the long-dashed curve in figure 2. The numerically generated Ω-values consistent with these solutions were $\Omega < 10^{-6}$ and $\Omega = 0.202$, respectively. These values agree with the above formulae, and document the above bifurcation. Also shown in figure 2 is a short-dashed curve representing the solution with $\kappa = 0.5$. This curve demonstrates the rotation of the steady salinity profile with decreasing κ inherent in (3.6). The location of the salinity maximum predicted by (3.6) is in excellent agreement with the numerical result.

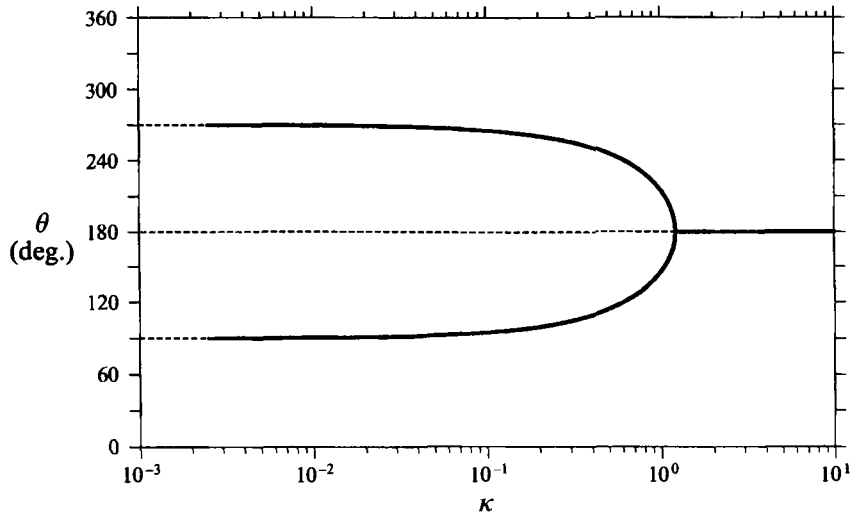

FIGURE 3. The loop oscillator bifurcation map for $\alpha = 0.0055$ and $\lambda = 0.015$, and with variable κ: non-dimensional diffusivity κ versus the location in degrees of the salinity maximum. The solid lines indicate stable solutions and the dashed curves indicate unstable solutions.

3.2. *Stability analysis in the limit of weak diffusion* (κ, α, $\lambda \ll O(1)$)

As κ decreases to small values, the salinity profile and angular velocity Ω_0 tend to the approximate values:

$$S = 1-(\lambda/\Omega_0)\sin\theta, \tag{3.7}$$

$$\Omega_0 = \pm(\lambda/2\alpha)^{1/2}. \tag{3.8}$$

Small perturbations to this state are governed by the linearized form of (2.12) where the basic state is as defined in (3.7). If we further assume that the salinity perturbation takes the form

$$S' = \mu_c(t)\cos\theta + \mu_S(t)\sin\theta,$$

the perturbed system is governed by

$$\dot{\mu}_c + \mu_S\Omega_0 - \Omega'\lambda/\Omega_0 = -\kappa\mu_c, \tag{3.9a}$$

$$\dot{\mu}_S - \Omega_0\mu_c = -\kappa\mu_S, \tag{3.9b}$$

$$\dot{\Omega}' = -\alpha\Omega' - \tfrac{1}{2}\mu_S, \tag{3.9c}$$

where the overdot implies a time derivative and the prime a perturbation.

The stability of the perturbation is judged in the usual way; namely, normal mode solutions in the form $\dot{q} = \sigma q$ are sought. The growth rates, σ, are governed by the cubic equation

$$(\sigma+\kappa)^3 + (\alpha-\kappa)(\sigma+\kappa)^2 + \frac{\lambda}{2\alpha}(\sigma+\kappa) + \frac{\lambda}{2\alpha}(2\alpha-\kappa) = 0. \tag{3.10}$$

Writing $\alpha = \lambda\hat{\alpha}$ and $\kappa = \lambda\hat{\kappa}$, we use a perturbation method to find the solution for $\sigma = \sum_{n=0}^{\infty}\sigma_n\lambda^n$. The three solutions for σ at lowest order are

$$\sigma_0 = 0, \quad \pm i(\lambda/2\alpha)^{1/2}. \tag{3.11}$$

The next correction for $\sigma_0 = 0$ is $\hat{\sigma}_1 = -2\hat{\alpha}-\hat{\kappa} < 0$; thus, this root is stable. For the imaginary roots, however, we obtain at $O(\lambda)$, $\sigma_1 = \frac{1}{2}\hat{\alpha}-\hat{\kappa}$; thus,

$$\sigma = \pm i(\lambda/2\alpha)^{1/2} + (\tfrac{1}{2}\alpha-\kappa) + O(\lambda^2). \tag{3.12}$$

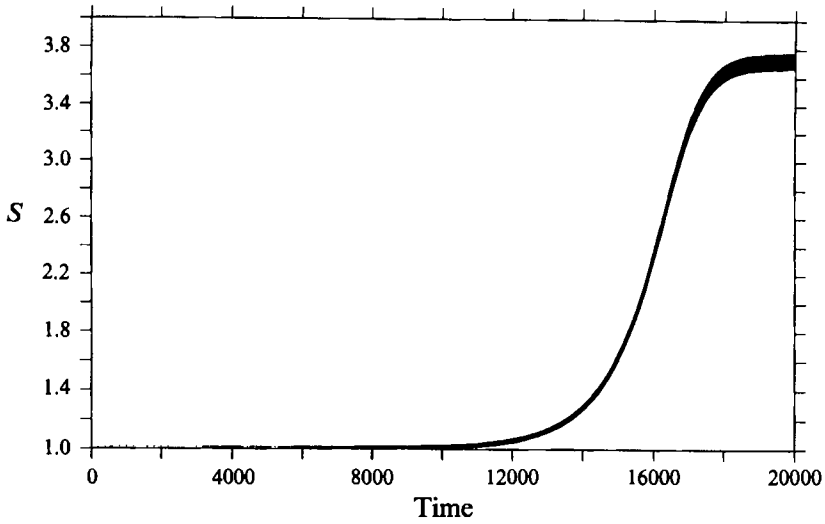

FIGURE 4. Temporal evolution of the salinity profile for $\alpha = 0.0055$, $\lambda = 0.015$ and $\kappa = 0.002$, close to the critical value defined by (3.12). Maximum salinity values are plotted as a function of time. The system was started from the inviscid equilibrium state.

The above demonstrates that the steady solution in (3.7) and (3.8) represents either an unstable or a stable centre, depending upon whether $\frac{1}{2}\alpha - \kappa$ is positive or negative, respectively. This analysis completes the bifurcation map shown in figure 3. The result in (3.12) is reassuring in that it recognizes κ as a stabilizing influence, but might be surprising in its apparent recognition of the viscosity α as destabilizing. In fact, it is the value of α relative to κ that matters, with the idea that low diffusivity is incapable of resisting the transition of the system from diffusively dominated behaviour, like that described above, to a state only weakly affected by diffusion.

Two other important points emerge from (3.12). The first is that the nature of the salinity perturbations is to be swept around the loop by the existing mean-state flow. This is evidenced by the appearance of $i\Omega_0$ in (3.12) (see (3.8) for the definition of Ω_0). The second point is that the decay (or growth) time of the perturbations ($T_d \approx (\frac{1}{2}\alpha - \kappa)^{-1}$) is entirely independent of the boundary forcing (represented by λ) and is sensitive only to the internal parameters of the system (α and κ). The only effect of the forcing is to set the advection scale. This differs greatly from the comparable stability characteristics appropriate to relaxation boundary conditions which, in turn, predict decay scales dependent on the boundary conditions ($T_d \approx 1/\Gamma$, where Γ is the relaxation parameter).

We have tested the above stability analysis using our numerical model. The model can be initiated using an arbitrary profile, an initial state of rest or the stationary inviscid solution (3.7). We present salinity profiles from two experiments, both with parameters $\alpha = 0.0055$, $\lambda = 0.015$, but differing in their values of κ, i.e. $\kappa = 0.003$ and 0.002 (see figures 4 and 5). In the first case with $\kappa = 0.003$, the system is just above its critical value defined by $\kappa_c = \frac{1}{2}\alpha = 0.00275$. Accordingly, we expect the system to attain the stable state defined by (3.7) and (3.8). The computed angular velocity for this experiment ($\Omega = 1.168$) is in excellent agreement with the theoretically expected value, and the salinity profile is roughly a simple cosine profile with the salinity extrema located at $\theta_0 = \frac{3}{2}\pi$ and $\frac{1}{2}\pi$ (see figure 5*a*). This experiment was started from rest and ran for 1000 time units. Ten profiles are shown, each separated by 100 time units. On the

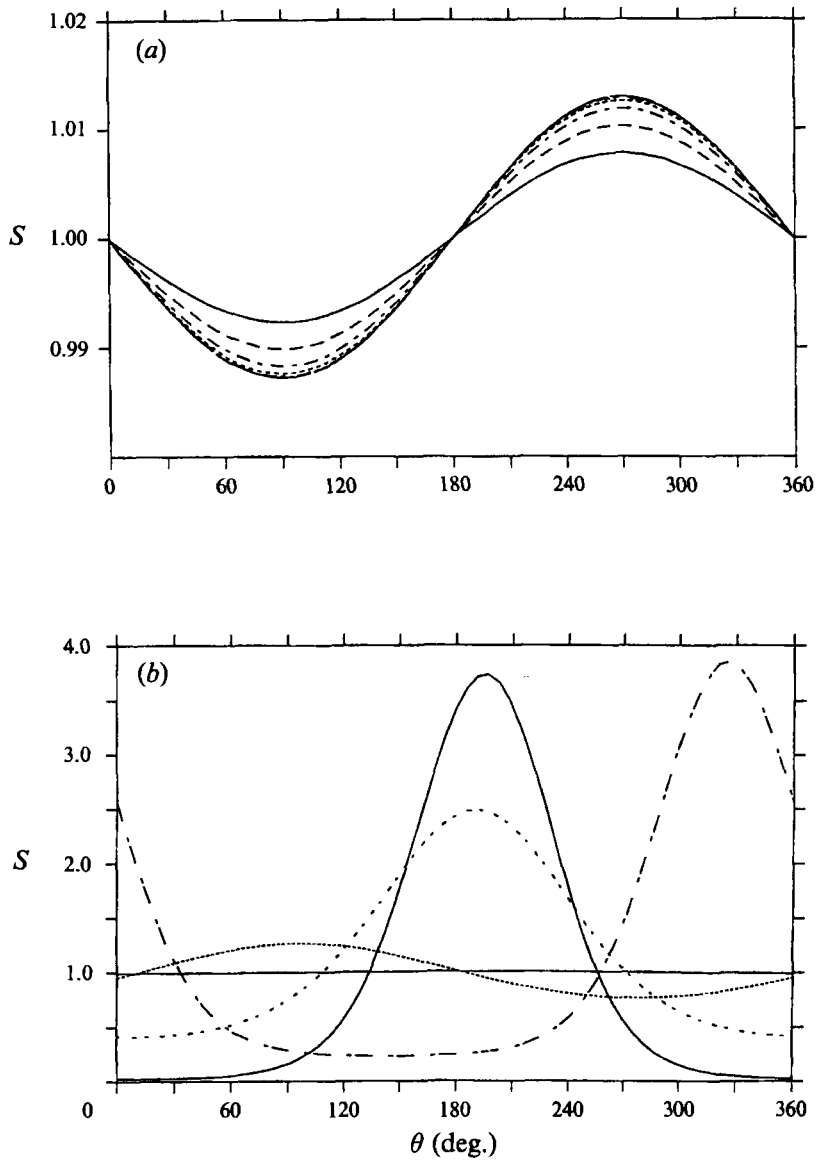

FIGURE 5. Salinity profiles of weakly diffusive solutions for $\alpha = 0.0055$, $\lambda = 0.015$, and (*a*) $\kappa = 0.003$, and (*b*) $\kappa = 0.002$. Note the great difference in salinity structures here, consistent with the expectations based on our stability analysis. The profiles in (*a*) indicate the system relaxation toward the steady profile. Ten profiles are plotted, each separated by 100 time units, the smallest amplitude being the earliest and the largest amplitude the final state. The experiment used a flat initial profile. The profiles in (*b*) are snapshots of a propagating pattern at $t = 10000$ (the solid line), $t = 14000$ (thin dotted curve), $t = 16000$ (heavy dotted curve), $t = 18000$ (dot-dashed curve), and $t = 20000$ (solid curve).

other hand, the spin-up process of the model takes much longer for the second case with $\kappa = 0.002$. It takes 20000 time units for this experiment, which began from the inviscid state defined by (3.7), to equilibrate, as shown in figure 4. For the first 10000 units of time, the salinity profile is almost indistinguishable from the solution in figure 5(*a*), although the cosine profile begins a slow propagation (compare the waves in

figure 5(*b*). Thereafter, the profile begins to change dramatically, as is seen in the large values of the salinity maximum found near time $T = 17500$, and in the later profiles of figure 5(*b*).

Several points need to be mentioned about figure 5. First, the final salinity profile in figure 5(*a*) is stationary, i.e. the system evolution from an arbitrary initial state is to approach the predicted profile (3.8). On the other hand, the system approaches a limit cycle for the second case, i.e. the profiles are in fact propagating. Secondly, there is clearly a major difference between results in figures 5(*a*) and 5(*b*), which in turn is consistent with the predictions of our stability analysis and generalizes the results beyond the special perturbations considered in (3.9). In combination with the first point, we identify the transition defined by (3.12) as a Hopf bifurcation. Finally, these profiles demonstrate that the salinity evolves into a spike-like function, indicative of a profound tendency found in this system to concentrate salt in one moving location. This appears in figure 5(*b*) in the amplitude of the salinity anomaly. The total maximum to minimum change obtains a value of 3.75. This is roughly 300 times the net change in salinity observed in the profile in figure 5(*a*). The difference between these results is all the more remarkable given that these experiments differ in one of the parameters by only 1×10^{-3}, such that the parameter straddles the Hopf bifurcation.

The minimum S-value in the experiment in figure 5(*b*) obtains a value of 0.03, representing relatively fresh water, and occupies a significant fraction of the loop. The tendency to produce a loop of nearly fresh water with all the salt concentrated in single intense plug is even more pronounced for κ-values slightly further from the Hopf bifurcation. We now proceed to consider the dynamics of such solutions.

3.3. *The non-diffusive limit – salt spike solutions*

We propose a test solution for the salinity profile in the form of a travelling delta function:

$$S = 2\pi\delta(\theta - \theta_0(t)), \tag{3.13}$$

where we have employed normalization to set the spike amplitude and δ denotes the usual Dirac delta function. The quantity θ_0 represents the azimuthal location of the spike and is potentially a function of time. Substituting (3.13) into (2.12) and neglecting κ yields the coupled set of ordinary differential equations

$$-2\pi\delta'\theta_0 + (\Omega + \lambda\sin\theta)\,2\pi\delta' = -2\pi\lambda\cos\theta\delta, \tag{3.14a}$$

$$\dot{\Omega} = -\alpha\Omega - \sin\theta_0, \tag{3.14b}$$

where δ' denotes the derivative of the delta function. If (3.14*a*) is multiplied by any periodic function of θ and integrated around the loop, it yields

$$\dot{\theta}_0 = \Omega + \lambda\sin\theta_0. \tag{3.14c}$$

We now consider the solutions of the set (3.14*b*, *c*).

Again, we are interested in small λ and α, so we consider an expansion in λ with $\alpha/\lambda = \hat{\alpha} = O(1)$. The lowest-order expansion yields

$$\dot{\theta}_0 = \Omega_0, \quad \dot{\Omega}_0 = -\sin\theta_0, \tag{3.15a, b}$$

where the subscript now refers to the order of the expansion. Equation (3.15*a*) shows that the spike follows the flow at leading order (this is consistent with the stability analysis discussed in the previous section). Equations (3.15) eventually yield a first integral, i.e.

$$\tfrac{1}{2}\dot{\theta}_0^2 - \cos\theta_0 = C, \tag{3.16}$$

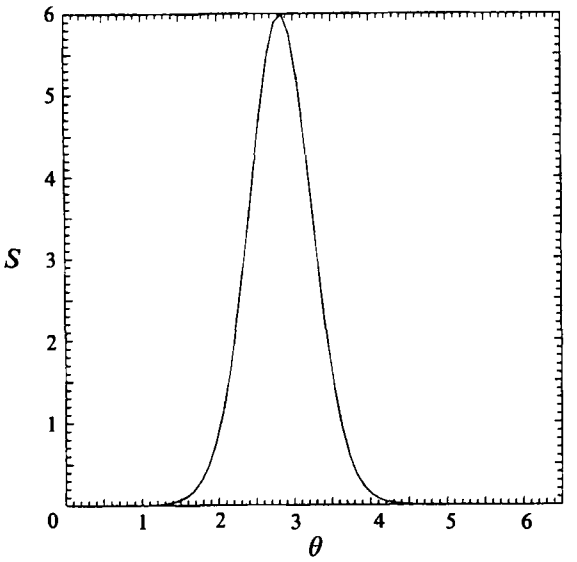

FIGURE 6. An example of a spike solution for $\alpha = 0.005$, $\lambda = 0.015$ and $\kappa = 0.001$. The maximum S-values are 6.0 and the minimum values are less than 0.001. Freshwater occupies most of the loop.

where the constant C is as yet unspecified. The above is the same equation as that of a nonlinear pendulum and its solution for θ_0 can in principle be written in terms of elliptic functions with free parameter C.

Forcing and dissipation appear in the next order of the expansion, which yields

$$\dot{\theta}_1 = \Omega_1 + \sin\theta_0, \quad \dot{\Omega}_1 = -\hat{\alpha}\Omega_0 - \cos\theta_0\theta_1. \tag{3.17a, b}$$

The above can be combined into

$$\ddot{\theta}_1 + \cos\theta_0\theta_1 = -\hat{\alpha}\Omega_0 + \cos\theta_0\dot{\theta}. \tag{3.18}$$

Some manipulation demonstrates that $\dot{\theta}_0$ is a solution of the adjoint operator of the left-hand side of (3.18). If attention is restricted to periodic solutions, one obtains the solvability condition

$$\hat{\alpha}\int_0^T \dot{\theta}_0^2\,\mathrm{d}t = \int_0^T \dot{\theta}_0^2\cos\theta_0\,\mathrm{d}t, \tag{3.19}$$

where T is the period of the oscillation, which, given (3.16), relates the unknown C to the system parameter $\hat{\alpha}$.

Equation (3.19) can in principle be applied for any $\hat{\alpha}$. It is clear from (3.16), however, that a critical value for C occurs when $C = 1$. This corresponds to the state where $\dot{\theta}_0 = 0$ when $\theta_0 = \pi$ or, recalling the pendulum analogy, the critical state dividing back-and-forth oscillations from those which complete full circuits about the loop centre. It is possible to evaluate (3.19) analytically for this case with the result that the critical $\hat{\alpha}$ at $C = 1$ is $\hat{\alpha} = 1/3$. For $\hat{\alpha} < 1/3$, the spike circulates the loop completely; for $\hat{\alpha} > 1/3$, the spike oscillates like a normal pendulum. It will be shown shortly that $\hat{\alpha} = 1/3$ represents a sort of period-doubling bifurcation.

It has been a remarkable result of our work that the spike solutions are realized in our numerical model. One example occurred in figure 5(*b*); another more extreme example occurs in figure 6. Here, $\alpha = 0.005$, $\lambda = 0.015$ ($\hat{\alpha} \equiv 1/3$) and $\kappa = 0.001$. The S-values in the spike are $O(6.0)$ and those in the great freshwater reservoir are

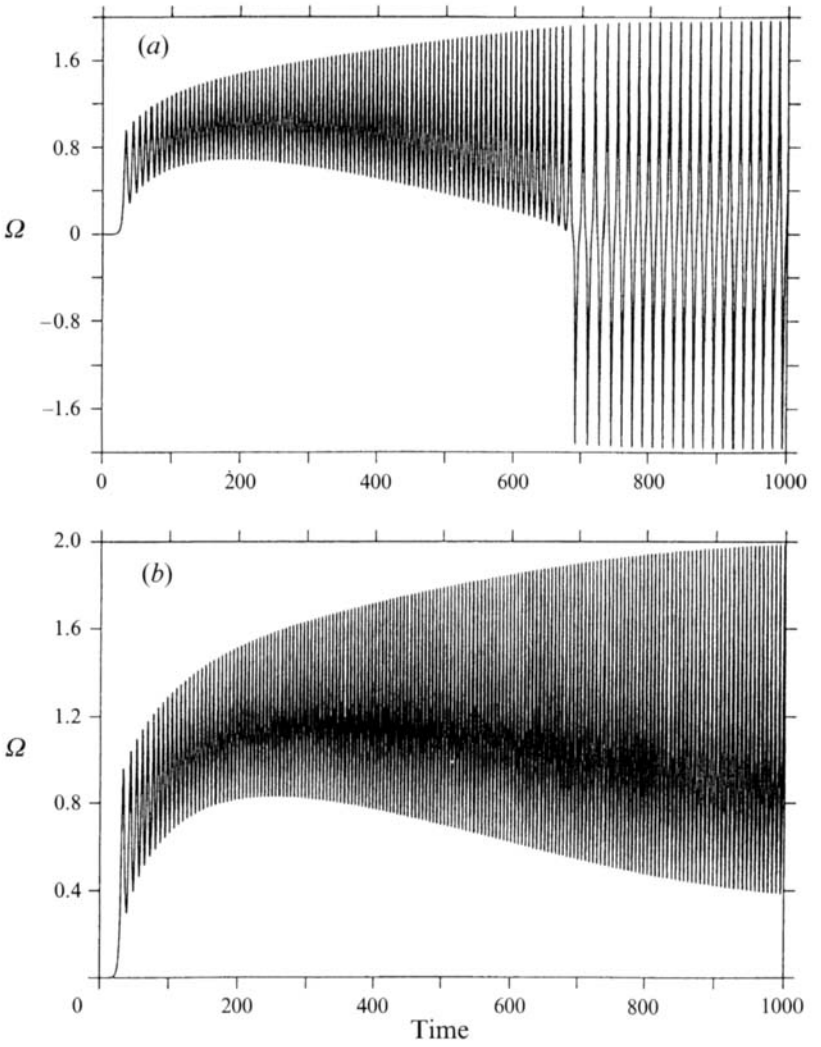

FIGURE 7. Temporal evolution of mean angular velocity for $\lambda = 0.015$, $\kappa = 0.0001$ and (*a*) $\alpha = 0.0055$, (*b*) $\alpha = 0.0045$.

numerically less than 10^{-3}. Further, the structure of the salinity profile is that of a very narrow almost Gaussian-like profile. We have demonstrated in a series of experiments that the widths and amplitude of this maximum are controlled by the employed value of κ. This appears if figures 5(*b*) and 6 are compared.

The temporal evolution of the angular velocity for parameter sets which straddle the period-doubling bifurcation has been determined by using our numerical model and their relative behaviours have been confirmed. Examples are shown in figures 7 and 8, both of which employ $\lambda = 0.015$, while $\kappa = 0.0001$ in figure 7 and $\alpha = 0.0055$ and 0.0045 in (*a*) and (*b*), respectively. Both experiments were begun from a state of rest. In figure 7(*a*), the early behaviour of Ω is to oscillate with purely positive values and with an increasing amplitude. Around $T = 680$, Ω passes through zero, and subsequently obtains values of both signs during each cycle. Note the approximate period doubling associated with the transition to pendulum-like behaviour at $T = 680$

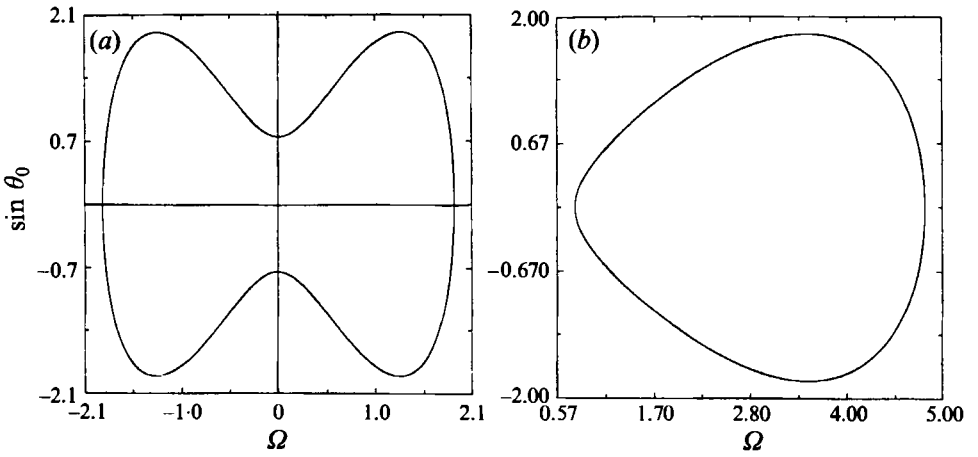

FIGURE 8. Phase-space diagrams for (*a*) $\alpha/\lambda = 0.34$ and (*b*) $\alpha/\lambda = 0.32$, and $\kappa = 0.001$. Note the butterfly structure in (*a*) consistent with a pendulum-like oscillation. The plot in (*b*), in contrast, is consistent with a one-signed value for Ω.

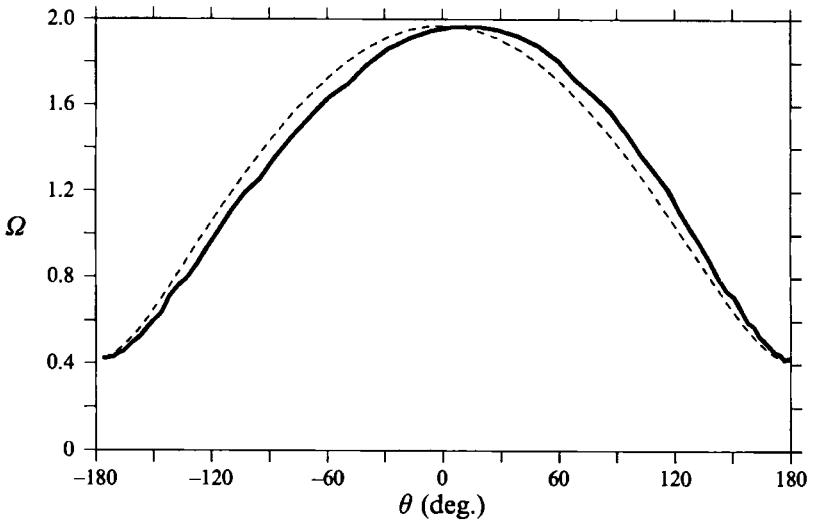

FIGURE 9. Phase relation between the mean angular velocity of the fluid (dashed curve) and angular velocity of the salinity maximum (solid curve) for $\alpha = 0.0045$, $\lambda = 0.015$, and $\kappa = 0.0001$.

(the periods were numerically determined to be about 11 for $T < 680$ and about 19 for $T > 680$). The latter part of the diagram corresponds to equilibrium behaviour for these settings. A different view of this pendulum equilibrium is given in figure 8(*a*), where a phase-space plot of $\dot{\theta}_0$ and $\sin\theta_0$ (i.e. angular velocity versus 'torque') is presented. Here, $\hat{\alpha} = 0.34$. Note the butterfly shape in figure 8(*a*), with both positive and negative values of $\dot{\theta}_0$.

The temporal evolution of Ω for $\hat{\alpha} < 1/3$ is shown in figure 7(*b*). Again, the early behaviour of Ω is to oscillate with positive values of an increasing amplitude, but the later behaviour indicates an asymptotic approach to an equilibrium with only positive Ω. The phase-space character of this equilibrium is shown in figure 8(*b*), ($\hat{\alpha} = 0.32$)

where it can be seen that the butterfly structure has been replaced by an ovular curve involving only positive Ω. This state corresponds to the continuous looping of the salt spike about the tube. Finally, visually comparing the equilibrated parts of figures 7(*a*) and 7(*b*) demonstrates the period-doubling phenomenon alluded to earlier. The reason for this is clearly that the pendulum-like oscillation in figure 7(*a*) has to transit the tube twice to complete a cycle, while the state in figure 7(*b*) must transit only once.

The physics maintaining the spike involves the nonlinear coupling of the advection of salt, whose rate is in turn set by the salt distribution and the freshwater flux profile. The latter generates a stationary secondary velocity field (see (2.4)). As shown in figure 9 water is moving counterclockwise, so that when the salinity maximum is on the left half of the loop, the gravitational torque accelerates the mean flow. The heavy saline blob thus moves rapidly through the precipitating bottom half, and hence does not experience much effect of the divergent secondary velocities. In contrast, the heavy blob slows as it nears the loop top and so experiences the evaporation-driven convergence there for a relatively long time. Note that although the mean angular velocity is symmetric with respect to $\theta = 0$ and π, the angular velocity of the salinity maximum is not. In fact, the salinity maximum moves slower than the mean fluid on the left branch of the loop, but it moves faster than the fluid on the right branch of the loop. These secondary circulations thus cause a concentration of the salinity profile; on the next oscillation, this tendency is reinforced. The only persistent opposition to this sharpening comes from diffusion which, being weak, yields very abrupt, spike-like profiles. The above-mentioned mechanics for the amplification of salinity perturbations is similar to those promoting the growth of thermal perturbations discussed by Welander (1967), but is slightly different from the positive feedback mechanism of a salinity anomaly in a thermally dominated meridional circulation discussed by Walin (1985).

3.4. *The relation of the oscillatory period to the forcing*

The results of Huang & Chou (1994) have motivated us to examine the dependence of limit-cycle periods on forcing. As discussed in the stability calculations of the previous sections, at leading order perturbations are simply advected; thus, the salinity oscillation period is determined by the mean current. According to (3.11), the period is thus proportional to $(\lambda/2\alpha)^{1/2}$. In dimensional units, this gives rise to a square-root dependence of the period on the precipitation/evaporation amplitude, i.e.

$$T = \left(\frac{E}{g\epsilon\beta\bar{S}}\frac{R}{r}\right)^{1/2}. \tag{3.20}$$

This is similar to the scaling analysis of Huang & Chou (1994). One may also analyse the spike solutions analytically in the limit of $C \gg 1$. There it may be demonstrated that the oscillation period behaves as $T \approx \lambda^{1/2}$, again a square-root dependence. In between, i.e. for small κ and $\hat{\alpha} \leqslant 1/3$, the frequency is most conveniently determined by numerical analysis. We have conducted experiments for $\alpha = 0.002$, $\kappa = 0.0002$ and several λ-values and the results are plotted in figure 10. The employed range of λ was from very near to the period-doubling boundary (~ 0.006) to well beyond that value. While the overall dependence is not inconsistent with a square-root behaviour, it is easy to believe that the graph could be interpreted as linear over much of this range. This is interesting because such a linear behaviour was reported by Huang & Chou (1994). We have also considered λ-values much larger than those shown here (up to $\lambda = 0.015$) and the square-root dependence eventually and unambiguously appears.

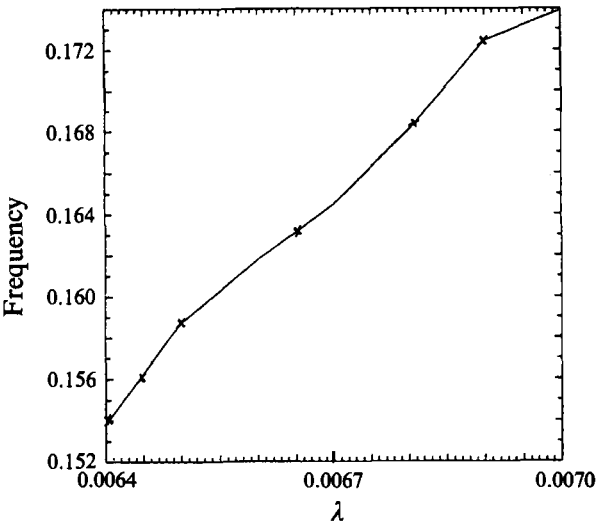

FIGURE 10. The dependence of oscillation period on forcing. In these experiments, $\alpha = 0.002$, and $\kappa = 0.0002$. The forcing parameter λ varies from 0.0059 to 0.007. The theoretically predicted bifurcation value is $\lambda = 0.006$; numerically it was found to be closer to 0.0058.

3.5. *System behaviour with other boundary conditions*

Given the sensitivity of oceanic GCMs to details of the boundary conditions and parameter settings, we are also interested in studying the impact of various boundary formulations on system behaviour. To this end, we have considered the effects of relaxation and virtual salt flux boundary conditions on the loop oscillator. Of course, natural boundary conditions are the 'correct' ones, and other conditions will be judged against them.

Relaxation conditions

Consider first the case of relaxation conditions, where for consistency the reference salinity S^* in (2.12*b*) has been chosen as the weakly diffusive stationary profile obtained using natural boundary conditions, i.e.

$$S^* = 1 - \frac{\lambda}{\Omega_0} \sin\theta. \tag{3.21}$$

Our analysis here somewhat mirrors the classical loop model studies of thermal convection subject to temperature relaxation (Keller 1966; Welander 1967), although, they employed relaxation profiles proportional to $\cos\theta$. Our profile is at right angles to this, and hence our results differ from those in past studies. The stationary solution corresponding to (3.21) is

$$S = -\frac{\gamma\lambda}{\Omega_0((\kappa+\gamma)^2+\Omega^2)}((\kappa+\gamma)\sin\theta - \Omega\cos\theta). \tag{3.22}$$

It is readily seen that when a strong relaxation condition applies, i.e. $\gamma \gg \Omega$, κ, this solution approaches the reference salinity profile (3.21); otherwise, there is always a difference between the reference salinity and the real salinity.

By repeating the analysis presented above for the case of natural boundary conditions, one can show that for a given sign of Ω_0, the system has one stationary

solution, in which the sign of Ω is the same as Ω_0; however, their values are different. The stability analysis gives rise to the lowest-order growth rate of the perturbation as

$$\sigma = -\gamma - \kappa, -\alpha. \tag{3.23}$$

There are two important points. First, the solution is stable, i.e. any perturbation would decay, as expected when the relaxation condition is imposed. Secondly, perturbations are not advected by the fluid. The non-advective nature of the perturbations is probably one of the most fundamental differences between models forced by relaxation conditions and natural boundary conditions.

Since a model with a strong relaxation condition on salinity has its limitations, it is interesting to examine the behaviour of the present system under a weak relaxation condition. Here we restrict attention to the parameter regime $\alpha, \lambda, \gamma \ll 1$, where $\gamma = T\Gamma$ measures non-dimensional relaxation time. In view of most model applications, we further order these parameters as $\alpha \sim \lambda \ll \gamma \ll 1$.

To leading order, the mean angular velocity is

$$\Omega = \gamma^{2/3} \Omega_0^{1/3}. \tag{3.24}$$

Recall that the natural boundary conditions give a loop fluid velocity of Ω_0. Clearly, the flow subject to relaxation conditions is very sensitive to γ, and tends to be small relative to the desired Ω_0.

The corresponding stationary solution (3.22) is reduced to

$$S = 1 - 2\alpha\gamma^{2/3} \Omega_0^{1/3} \sin\theta + 2\alpha\Omega_0^{2/3} \gamma^{1/3} \cos\theta, \tag{3.25}$$

where it is clear that the last term is the leading-order correction. Regardless of the value of γ, S does not converge to S^*, a somewhat surprising and counter-intuitive result.

The equivalent 'salt flux' associated with relaxation boundary conditions is to leading order proportional to S^* in this problem, i.e.

$$-\gamma(S - S^*) \approx -\gamma\left(2\alpha\Omega_0^{2/3} \gamma^{1/3} \cos\theta + \frac{\lambda}{\Omega_0} \sin\theta\right), \tag{3.26}$$

where it is seen that the latter term dominates. If this is compared with the virtual salt flux formulation, (2.6*b*), it is seen to be 90° out of phase with that flux.

Finally, the growth rate of perturbations to the steady solutions turns out to be

$$\sigma = \pm i\Omega - \gamma + O(\gamma^2, \alpha, \lambda), \tag{3.27}$$

demonstrating a decay rate controlled by the relaxation parameter. The imaginary part shows that, while decaying, the perturbations move with the mean flow. As one would expect, solutions under weak relaxation conditions cannot match the reference salinity. In fact, most quantities, such as the mean angular velocity, the virtual freshwater flux diagnosed from the model, are distorted.

The above results represent quantitative differences between relaxation and natural boundary condition behaviour. It is perhaps equally important that qualitatively the relaxation conditions prevent spike formation entirely for the reason that they restrict the salinity profile to have a shape like that of the imposed boundary conditions. In some sense, this implies a rather severe departure from physical behaviour.

Virtual salt flux (VSF) conditions

The loop oscillator salt equation subject to the usual VSF condition is (2.6*b*). This equation, while standard in form, employs in fact a modified version of the true boundary condition in that $\bar{S}$ appears rather than S. Local flux is thus proportional to

globally averaged salinity, rather than local salinity. This boundary condition employing $\bar{S}$ is now widely accepted because it ensures global conservation of salt and in practice prevents the occurrence of the so-called 'salt explosion', in which net global and local salt values grow without bound.

Regarding steady solutions, VSF conditions perform in a much more acceptable fashion than relaxation conditions. Namely, the steady profiles and velocities consistent with small α and λ are good approximations to those for natural boundary conditions. The stability properties for the steady solutions are also comparable, with a stability boundary characteristic of a Hopf bifurcation occurring when $\frac{1}{2}\alpha - \kappa$ changes sign.

The same cannot be said for the limit-cycle solutions of (2.6*b*) when compared to those generated by natural boundary conditions. The VSF form of the loop oscillator lends itself readily to analytical analysis; the details appear in Appendix A and the methods are similar to those appearing earlier.

The principal differences remarked on here are both qualitative and quantitative. First, VSF conditions prevent spike formation; rather, salinity profiles are constrained to be low mode in structure. The reasons for this are related to the elimination of some of the nonlinear terms in the salt equation associated with natural boundary conditions. The convergence mechanisms responsible for profile sharpening in particular are removed. Secondly, we have been unable to locate any parameter settings which generate a complete loop oscillation for VSF. Rather, all limit-cycle oscillations are of the regular pendulum type, like that in figure 8(*a*). We now have considerable numerical evidence in support of this result although the reasons for it are unclear. At the very least, it can be said that the nature of the loop oscillator variability is very sensitive in unphysical ways to VSF conditions. Thirdly, VSF conditions in the loop oscillator can generally lead to the very unphysical generation of negative salinities in their limit-cycle solutions. The reason for this is the significant quantitative error in the flux specification associated with the replacement of the local salinity value by a global average salinity in the boundary condition. As a result, flux is grossly overestimated for low salinities and underestimated for high salinities. There is no guarantee that low salinity values will not be pushed to negative values. Natural boundary conditions, in contrast, have an effective flux proportional to local salinity; therefore, low salinities are associated with ever-decreasing fluxes. Salinity always remains positive. We should also remark that in experiments with the 'true' specification of virtual salt flux, in which $\bar{S}$ in (2.6*c*) is replaced by S, we have been unable to obtain physical behaviour. Rather, a loop oscillator version of the salt explosion occurs because salt conservation is no longer guaranteed.

4. A thermohaline loop model

We now move on to consider convection in a fluid whose density is set by both heat and salinity. Again a central motivation in our analysis is to examine the impact of the natural boundary conditions in this system; however, we also feel that models like this are of relevance to climate. The history of climate theory includes notable contributions from the study of simple process models, many of which are of the box model variety alluded to earlier. While the present loop model represents a step forward in terms of complexity, we are nonetheless motivated to draw parallels between our results and those of the original box model of Stommel, with a view to clarifying box model parameterizations and emphasizing new results. A brief review of Stommel's results will serve to set the stage.

Stommel's model was of two boxes connected to each other by pipes, and to heat and

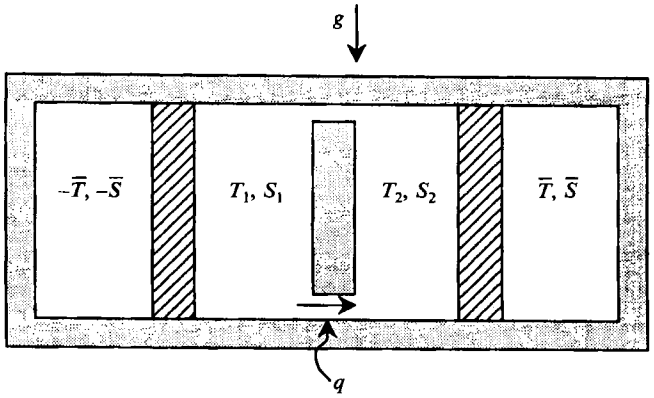

FIGURE 11. Stommel box model schematic. Two neighbouring well-mixed boxes exchange fluid by means of pipes. This advective exchange rate is proportional to the relative densities of the boxes. In addition, both boxes exchange heat and salt with infinite reservoirs at $\bar{T}$ and $\bar{S}$ according to relaxation laws. Gravity acts downward. Note that the forcing fields in figure 1 are configured to resemble the reservoir distribution here. The fluid is heated on the right, so a positive circulation corresponds to hot fluid rising and is referred to as a thermally direct cell. A high-salt reservoir also sits on the right (corresponding to an evaporation zone in figure 1). Hence, a negative circulation corresponds to salty fluid sinking and will be referred to as a saline mode.

salinity reservoirs by conductive interfaces (see figure 11). The fluid exchange rate between the two well-mixed boxes was proportional to the density difference between them. Property exchange between the reservoirs and the fluid occurred by relaxation, with the salinity timescale assumed much longer than the heat timescale. The equations governing this system can be effectively obtained from (2.12) by finite differencing the advective derivatives, suppressing momentum acceleration, suppressing λ, and (most importantly) suppressing heat and salinity diffusion. It is also necessary to add a relaxation term, $\gamma_S(S-S_r)$, to the salinity equation (2.6) and to assume antisymmetric solutions. Stommel computed the steady solutions of his system which he was able to reduce to a nonlinear equation with the flux between boxes as the independent variable. This equation in our notation is

$$A\hat{\Omega} = \frac{1}{(1+\delta|\hat{\Omega}|)R} - \frac{1}{(1+|\hat{\Omega}|)}, \tag{4.1}$$

where $A = \alpha\gamma$, $\hat{\Omega} = \Omega/\gamma$, δ represents the ratio of thermal relaxation time to our *ad hoc* salinity relaxation time and R here is given by $\beta\bar{S}/\alpha\bar{T}$. This equation Stommel solved graphically and a synopsis is given in figure 12. The y-axis is gravitational torque τ (essentially the right-hand side of (4.1)), which is plotted as a function of flux ($\hat{\Omega}$). The two curves in figure 12(*a*) are of net gravitational torque for $\delta = 1$ and $\delta = 1/6$, i.e. for identical heat and salinity relaxation times and for salinity relaxation time long compared to heat relaxation time ($R = 2$ in both). The straight line represents friction (i.e. the left-hand side of (4.1)) for a given A and the intersection of the frictional and gravitational curves constitutes a solution of (4.1). The three curves in figure 12(*b*) are plots of torque for three different values of R, namely 2, 1, and 0.5 ($\delta = 1/6$ in all three). The first R corresponds to the value discussed by Stommel and we include the others for completeness. The straight line again represents friction.

It is clear from figure 12(*a*) that different relaxation times raise the possibility of multiple equilibria. The convention here is that positive $\hat{\Omega}$ denotes a thermally direct mode (i.e. hot water rising), so that if $\delta < 1$ thermally direct and saline direct (salty

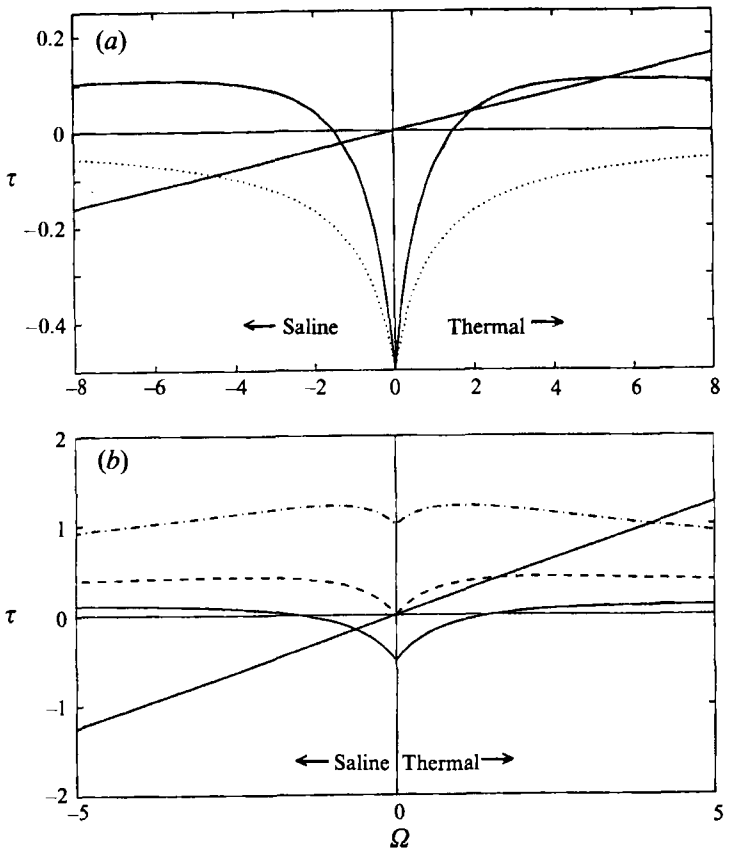

FIGURE 12. Box model solutions: net gravitational torque (τ) and friction torque versus angular velocity Ω. Solutions are found at the intersection of the frictional line and the solid gravitational curves. The curves in (a) are for identical relaxation times ($\delta = 1$, dotted) and slow salt relaxation ($\delta = 1/6$, solid); $R = 2$ in both. Multiple equilibria occur for $\delta < 1$. In (b) $\delta = 1/6$, but $R = 2$ (solid), 1 (dashed) and 0.5 (dot-dashed). Multiple equilibria exist, but their nature depends upon the value of R relative to 1.

water sinking) cells potentially can exist. Whether they in fact occur clearly depends on A: small A (weak friction) increases the likelihood of multiple solutions. On the other hand, if $\delta = 1$, the system can only exhibit a saline mode (recall that $R = 2$ in these plots). Figure 12(b) demonstrates that the nature of the equilibria also depend on R. Analysis demonstrates that multiple equilibria exist if $1/\delta > R \geqslant 1$. One of the solutions for $R = 1$ corresponds to $\hat{\Omega} = 0$ and the other to a thermally direct mode. The stagnant solution is a disguised saline mode; the lack of motion allows the slow salinity effects to control density. Finally, for $R < 1$, only thermal modes exist while for $R > 1/\delta$, only saline modes exist. The physical mechanisms responsible for this behaviour are clearly illustrated in Appendix B, where a modified box model, based on freshwater flux rather than salinity relaxation or virtual salt flux, is discussed. This model first appeared in Huang, Luyten & Stommel (1992).

This review, among other things, emphasizes two novel effects that the loop oscillator can include in a simple thermohaline model, namely diffusion and explicit freshwater flux. Note that nothing like κ_T or κ_S appears in the Stommel model. (Thual & McWilliams 1992 discuss the inclusion of a diffusion parameterization in a box

model, but find it does not importantly influence their results.) Indeed, it might even be argued that diffusive exchanges are inappropriately represented in a model consisting of two perfectly mixed, but separated vessels. With regard to freshwater flux, nothing like a salinity relaxation parameter occurs in the loop oscillator, and we instead must appeal to the explicit representation of surface exchange and model physics to internally determine the timescales of salinity response.

4.1. *Steady solutions*

Bearing the above points in mind, we now consider analytical solutions for the loop oscillator. We fix the value of θ_p at $-\frac{1}{2}\pi$ and θ_T at $\frac{1}{2}\pi$, giving the forcing fields shown in figure 1. This aligns the regions of strongest heating with those of evaporation, which is intuitively plausible. This restriction is of course not necessary, but in some sense results in the closest analogy between the loop oscillator and the classical box model and facilitates comparisons.

We first consider steady solutions of (2.12). The exact solution of (2.12*a*) is obtained by first integrating once in θ, i.e.

$$(\Omega+\lambda\cos\theta)\,S=\kappa_S S_\theta+C. \tag{4.2}$$

The constant C can be determined as a solvability condition by applying the boundary condition of periodicity; thus,

$$C=\langle(\Omega+\lambda\cos\theta)\,S\rangle. \tag{4.3}$$

Equation (4.2) is a first-order equation and can be solved by use of an integrating factor. The exact form for S is thus

$$S=C\,\mathrm{e}^{(\Omega\theta+\lambda\sin\theta)/\kappa_S}\int_0^\theta \mathrm{e}^{-(\Omega\theta'+\lambda\sin\theta')/\kappa_S}\,\mathrm{d}\theta'+S(0)\,\mathrm{e}^{(\Omega\theta+\lambda\sin\theta)/\kappa_S}, \tag{4.4}$$

where $S(0)$ is currently unknown and C is set by (4.3). Using (4.4) to evaluate (4.3) gives the solution for salinity as

$$S=S(0)\,\mathrm{e}^{(\Omega\theta+\lambda\sin\theta)/\kappa_S}-\frac{S(0)\,\kappa_S\langle\mathrm{e}^{-\Omega\theta/\kappa_S}\rangle}{\Omega\langle\mathrm{e}^{-(\Omega\theta+\lambda\sin\theta)/\kappa_S}\rangle}\mathrm{e}^{(\Omega\theta+\lambda\sin\theta)/\kappa_S}\int_0^\theta \mathrm{e}^{-(\Omega\theta'+\lambda\sin\theta')/\kappa_S}\,\mathrm{d}\theta', \tag{4.5}$$

where $S(0)$ is determined by the normalization constraint $\langle S\rangle=1$. Equation (4.5) applies for any Ω. The approximate form of (4.5), valid for small λ/κ_S, is obtained by expanding the appropriate exponentials in Taylor series:

$$S(\theta)=1+\frac{\lambda}{\kappa_S}\left(\frac{\kappa_S^2}{\Omega^2+\kappa_S^2}\sin\theta-\frac{\Omega\kappa_S}{\Omega^2+\kappa_S^2}\cos\theta\right)+O\left(\frac{\lambda}{\kappa_S}\right)^2. \tag{4.6}$$

Since we are considering the case where $\gamma\gg\lambda$, κ_T, a perturbation expansion in λ is used to solve (2.12*b*). The result is

$$T=\frac{-\gamma\Delta\Omega}{\Omega^2+(\gamma+\kappa_T)^2}\cos\theta+\frac{(\gamma+\kappa_T)\gamma\Delta}{\Omega^2+(\gamma+\kappa_T)^2}\sin\theta+O(\lambda^2). \tag{4.7}$$

Using (4.6) and (4.7) to evaluate the gravitational torque in (2.12*c*) gives the equation

$$\alpha\Omega=-\frac{\lambda\kappa_S}{2(\Omega^2+\kappa_S^2)}+\frac{(\gamma+\kappa_T)\gamma\Delta}{2R(\Omega^2+(\gamma+\kappa_T)^2)}+O\left(\frac{\lambda}{\kappa_S}\right)^2, \tag{4.8}$$

from which Ω can be numerically computed as a function of λ, κ_T, κ_S, α and γ. However, it turns out to be particularly illuminating to solve (4.8) graphically.

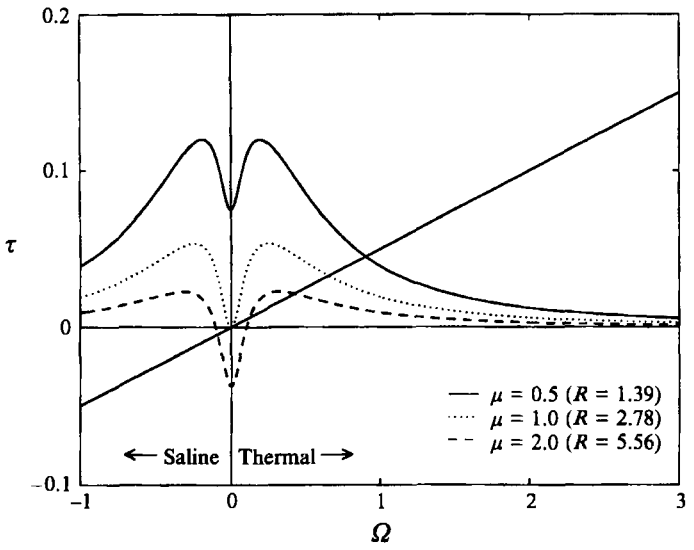

FIGURE 13. Loop model solutions: gravitational and frictional torques versus angular velocity. Frictional torque is represented by the straight line and gravitational torque by the curves. The three curves denote $\mu = 2$, 1 and 0.5. The slope of the frictional torque is $\alpha = 0.05$. The graph is similar to that in figure 12(*b*).

To facilitate this, we define an effective density ratio

$$\mu = \frac{\lambda R(\gamma + \kappa_T)}{\kappa_S \gamma \Delta} \tag{4.9}$$

and an effective relaxation timescale ratio

$$d = \frac{\kappa_S}{\gamma + \kappa_T}. \tag{4.10}$$

Consider now the behaviour of the right-hand side (RHS) of (4.8) as a function of Ω. For $\Omega = 0$, we have

$$\mathrm{RHS}(\Omega = 0) = \frac{\lambda}{2\kappa_S} \frac{1-\mu}{\mu}, \tag{4.11}$$

while for large $\Omega (\Omega \gg \gamma, \kappa_S, \kappa_T)$,

$$\mathrm{RHS}(\Omega \to \infty) \to \frac{\lambda \kappa_S}{2\Omega^2} \frac{1}{\mu} \left(\frac{1}{d^2} - \mu \right). \tag{4.12}$$

The torque for large Ω is positive if $\mu < 1/d^2$. In contrast, the torque for $\Omega = 0$ is positive, zero or negative if μ is less than, equal to or greater than 1, respectively. A torque zero crossing is anticipated for $1/d^2 > \mu > 1$ (we are working in a regime where $d < 1$) and can be shown to occur at

$$\Omega_c^2 = \frac{(\gamma + \kappa_T)^2 (\mu - 1)}{(1/d^2) - \mu}. \tag{4.13}$$

Note that $\Omega_c \to \infty$ as $\mu \to 1/d^2$.

The essential features of the torque function can be deduced from the above, from which it is seen that the parameters μ and d play a central role. Graphical examples appear in figure 13, with the curves denoting torque and the straight line friction. As

in figure 12, the intersection of the curves and the straight line represents a solution of (4.8). Also, the convention of figure 13 is that positive Ω denotes a thermally direct mode (cold fluid sinking) and negative Ω denotes a saline direct mode (salty water sinking).

The three curves plotted in figure 13 correspond to $\mu = 0.5$, 1 and 2. It is clear that $\mu > 1$ potentially yields multiple equilibria consisting of both types of cells and that the saline mode (negative Ω) is persistently smaller in magnitude than the thermally direct cell. It is less obvious, but nonetheless true, that $\mu < 1$ can also yield multiple equilibria over a limited range of frictional parameters. The nature of the torque curve in this case is such that the allowable Ω-values are all positive; however, one is much smaller in magnitude than the other. We will argue shortly that this weaker root represents a disguised saline mode, in spite of its positive value.

Taken as a whole, the structure of figure 13 is remarkably similar to figure 12(*b*) and encourages us to identify analogous parameters between the two formulations. The obvious comparisons are between μ in (4.9) and R as defined in Stommel's model, and d in (4.10) and the heat-to-salinity timescale ratio, δ, of Stommel's model. Note how varying μ relative to a value of 1 leads to the same type of multiple equilibria behaviour as does the R variations in figure 12(*b*). Note also that $d < 1$ leads to a finite range for μ over which a true saline mode ($\Omega < 0$) develops. Figure 12(*a*) demonstrates this same behaviour as a function of δ.

These identifications yield some interesting and enlightening results. First, in his box model, Stommel based the density ratio, R, on the extreme values of temperature and salinity found in his reservoirs. In our loop model, we have formed a comparable density ratio from the volume-averaged salinity $\bar{S}$ and total temperature range $\bar{T}_0$. The dynamically significant density ratio, μ, differs considerably from R, but may be understood in the following way.

We might anticipate that the forced and diffusive variations of salinity in our loop would be $O(\lambda/\kappa_S)$ from (2.12*a*) (upon ignoring Ω). Certainly, this is consistent with (4.6) if $\Omega = 0$, and represents a dynamical scaling for salinity. Ignoring advection in the heat equation similarly yields a temperature variation estimate of $\gamma\Delta/(\gamma+\kappa_T)$. Combining these demonstrates that an appropriate density ratio based on temperature and salinity variations is then $\beta\bar{S}\lambda(\gamma+\kappa_T)/(\alpha\bar{T}_0\kappa_S\gamma\Delta)$, which is precisely our definition of μ and supports its interpretation.

The role of the timescale ratio δ in Stommel's model is played here by $d = \kappa_S/(\gamma+\kappa_T)$: $d < 1$, which is consistent with the Stommel analysis, is due in large part to the strong negative feedback physics encapsulated in γ. What is interesting is that the role of the salinity relaxation time is played by κ_S which, in turn, is entirely independent of boundary exchange processes. A similar result was noted in the case of purely saline loop discussed in §3, where the timescale of salinity anomalies was also found to be independent of the surface boundary parameterization.

While the notion that $\delta < 1$ in Stommel's model finds support here, the notion that $R > 1$ bears some revisiting. Our effective density ratio μ involves a number of quantities whose values are not well known. While $\beta\bar{S}/\alpha\bar{T}_0 \approx 4$ seems reasonable, the relative value of, for example, λ/κ_S is not known well enough to guarantee the size of μ relative to 1. It seems advisable to consider all possibilities for μ.

Another important point implied by figure 13 is that the saline and thermal modes are impossible in certain regimes of the effective density ratio μ. For $\mu < 1$ there is no stable saline solution, but there is always a stable thermal solution. For $\mu > 1$ there is always a stable saline solution; however, for A larger than a certain critical value there is no stable thermal solution. The non-existence of either the thermal or saline mode

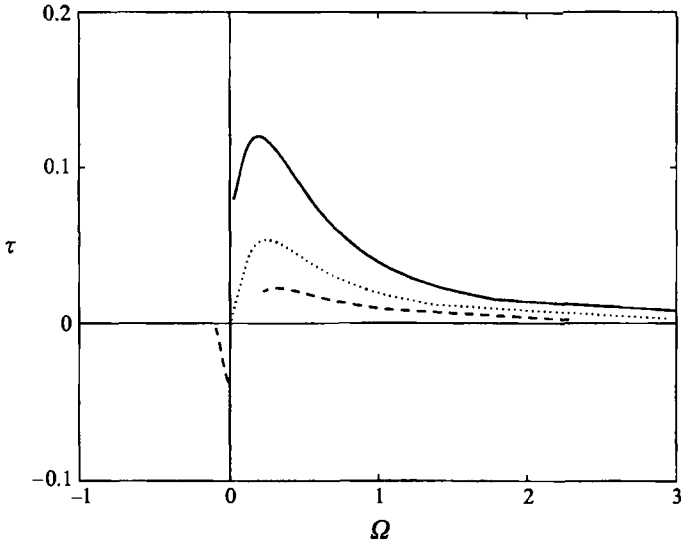

FIGURE 14. Numerical results: as figure 13 except that the solutions have been numerically generated. Blank areas denote zones of instability. Where available, the solutions closely resemble those in figure 13. $\kappa_T = \kappa_S = 0.1$, $\gamma = 0.5$ and $\lambda = 0.015$.

resembles the situation in the Stommel (1961) box model. It is interesting to note that strong freshwater flux also causes the thermal mode to collapse in two- and three-dimensional thermohaline circulation models. The stability boundary of the thermal mode in these oceanic general circulation models is very difficult to predict. The exact stability boundary of the thermal mode for a box model can be calculated, in principle, by the approach discussed in Appendix B. However, in the present case, this approach yields a cumbersome cubic equation. Nevertheless, this stability boundary is closely related to the effective density ratio $\mu = \lambda R(\gamma + \kappa_T)/(\kappa_S \gamma \Delta)$, with larger μ favouring stable saline modes only. Since μ is linearly proportional to the freshwater forcing, if other parameters are fixed, an increase in λ will eventually lead to a catastrophic transition from the thermal mode to the saline mode.

4.2. *Numerical solutions and stability*

It remains for us to test several aspects of the above solutions. First, the above analysis implicitly assumes that a steady-state assumption is justified. Our attempts at a stability analysis have also failed to yield clear characterizations. It is useful to consider such issues by numerical methods.

Perhaps the most significant prediction of the previous subsection is the sensitivity of the loop behaviour to the value of μ. In figure 14, we present the results of related sets of numerical experiments. Several lines appear on figure 14 and each refers to a given set of experiments as follows. The parameters $\kappa_S = \kappa_T = 0.1$, $\gamma = 0.5$ and $\lambda = 0.15$, and are fixed in all experiments. (Note that $\kappa_T = \kappa_S$ here: while there are some interesting solution characteristics which depend upon $\kappa_T \neq \kappa_S$, we choose to focus as clearly as possible on the effect of the different boundary conditions on temperature and salinity by assigning the two diffusions the same value. This will be true of all the experiments described here.) A value of R was then chosen and our numerical loop model was integrated to a steady state (assuming one existed) for a wide variety of α-values. This experiment was repeated for several different R-values and initial

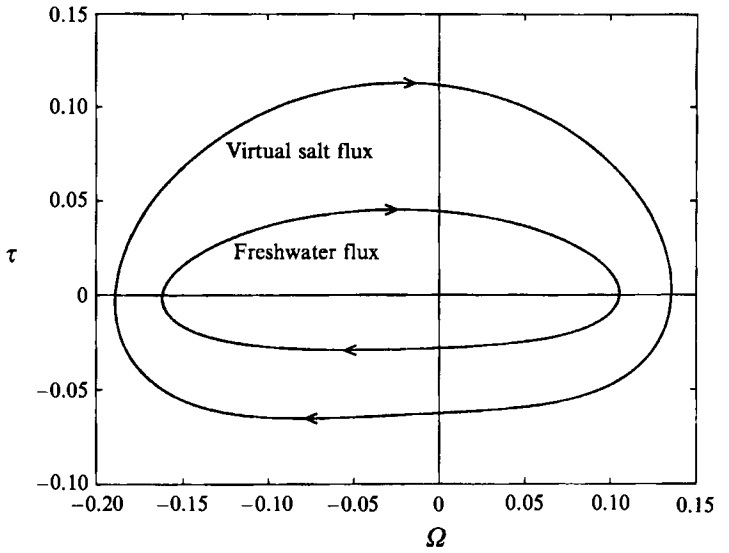

FIGURE 15. Saline limit cycle: gravitational torque versus angular velocity. All parameters here are fixed, thus the plot is of a limit cycle. Note that the Ω-values are relatively weak and of both signs. Calculations using both natural and virtual salt flux boundary conditions are shown. The arrows indicate the direction of the oscillation.

conditions, thereby hopefully locating any available solutions, steady or transient. Net torque of the stationary solutions is plotted against Ω; hence, figure 14 is analogous to figure 13.

The reason for varying R is that this procedure provides a simple way of varying μ. The displayed R values are $R \approx 1.4$, 2.8 and 5.6, corresponding to $\mu = 0.5$, 1 and 2. We also mention that in tests where the other parameters were varied such that they obtained the above μ-values, the results in figure 14 were replicated, provided that λ/κ_S was small.

Note that many of the essential ingredients of the analytical solutions appear here, as well as some essential distinctions. Most importantly, both thermal and saline direct cells appear for $\mu = 2$. This is consistent with our earlier analysis. The torque curves are discontinuous, however. For example, the $\mu = 2$ line stops at a value of $\Omega \sim 0.2$, and no values are plotted for $0 < \Omega < 0.2$. The reason for this is that the thermally direct mode is numerically unstable for these Ω-values. Referring again to figure 13, regimes in which multiple equilibria are possible actually possess three solutions. It is always the case that two of these solutions are thermally direct and one is saline. Of the thermal modes, one is considerably weaker than the other. In figure 14, these weak modes occur for the Ω-range in question and our results here constitute numerical evidence that these solutions are unstable. We find numerically that, as α increases, thermal modes spontaneously flip to saline modes at a critical value. At this point, starting from the saline mode, increases or decreases of α result in saline cell solutions. Stommel (1961) was able to explicitly calculate the stability of his multiple equilibria; our results here are entirely analogous to his.

The results for $\mu < 1$ are also in agreement with our analytical expectations. Note that only thermal modes are available. This differs from the earlier $\mu > 1$ case, in which solutions exist for all Ω. More than one solution also occurs for certain α-values if μ is only slightly less than 1. (In this case, the analytical solution shows that the

gravitational torque at $\Omega = 0$ is very small and the structure of the curve is flat. An appropriate value for α results in the frictional torque line intersecting the gravitational torque curve three times, all on the positive-Ω side. As before, the middle solution is unstable. Numerically, we only see the smallest and largest Ω-solutions.) The case of μ slightly less than 1 thus exhibits the interesting feature of multiple stable thermally direct cells. It is clear from the curve, however, that one of these two modes has a considerably weaker Ω-value associated with it. Further, we find that the temperature structure of these modes is always roughly the same as the boundary temperature profile. (Note that this is in keeping with (4.7).) Such weak overturning coupled with a maximum temperature effect is only possible if salinity is a dominant factor in determining density. The impact of the salinity is in turn enabled by the sluggishness of the flow. Thus, we see that the weaker thermally direct solution here is in reality a saline mode, disguised by a thermally direct velocity field, which in turn exists because of the details of the parameters.

We could have also plotted in figure 14 the analytical curves for comparison to the numerical results. This we have not done because no new information is added: the two curves are virtually indistinguishable.

Thus we conclude that this series of tests supports the previous analytical solutions. We also mention that $\lambda/\kappa_S = 0.15$ (as it is here) is also not very small, thus hinting at the robustness of the results.

4.3. *A saline mode limit cycle*

The attractor basins for the steady solutions of the Stommel model apparently occupy all of the phase space; the only time dependence the system admits occurs during transitions from one state to the other. These in turn generally require sizable perturbations to initiate. It is of interest that our system displays a self-sustaining oscillation, and we now describe its properties.

Figure 15 is an example plot of the limit cycle of the loop oscillator. The plot is of torque versus Ω. The parameters appropriate to this experiment are $\lambda = 0.015$, $\gamma = 0.5$, $\alpha = 0.01$, $\kappa_S = \kappa_T = 0.04$, and $R = 2.0$, yielding an effective density ratio of $\mu = 1.1$. Thus, multiple equilibria are available according to the analysis of the previous section. Note that the Ω-values in figure 15 are small in magnitude and both signs appear. The former fact suggests that the limit cycle reflects saline mode dynamics. Indeed, if the loop oscillator model is started from appropriate initial conditions for these same parameters, the system approaches a steady thermally direct cell whose magnitude is captured by the preceding steady-state analysis.

Another curious feature of this limit cycle is its dependence on diffusion. For all other parameters fixed, we find first the appearance of steady saline modes as diffusion decreases (and thus as μ increases beyond 1), followed by the onset of the limit-cycle dynamics for smaller $\kappa_S = \kappa_T$, and thence back to a steady saline mode for yet smaller $\kappa_S = \kappa_T$. The parameters used for the limit cycle in figure 15 exhibit the first transition at about $\kappa_S = \kappa_T = 0.04$. The collapse back to a steady saline mode occurs at $\kappa_S = \kappa_T = 0.01$. These transitions have been determined numerically; our attempts to define the stability boundaries analytically have failed.

To explain the oscillation dynamics, and the above transitions, it is useful to recall the results in §3 regarding the nature of 'spike-like' salinity profiles in the loop in the presence of weak diffusion. The tendency there is for salinity to collect at preferred locations owing to the effects of evaporation-driven convergence.

Here, the initial onset of steady saline modes occurs for strong enough diffusions that the salinity profiles remain relatively spread throughout the loop; however,

reductions in the diffusion allow the salinity anomalies to grow in magnitude. Consider now the sequence of events in the limit-cycle parameter regime, beginning with the growth of a positive salinity anomaly. First, since the motion is slow, the thermal contribution to the torque is essentially always at its maximum and acting to accelerate the flow in a positive direction. However, as the salinity anomaly grows under the evaporative side of the forcing, it eventually controls the net torque and negative circulation develops. The salinity anomaly goes with it, thus moving into regions of less-intense convergence (and possibly even divergence). Diffusion is then able to more effectively spread the anomaly, thus reducing its amplitude and its effect on net torque. Inertia causes the fluid to overshoot its equilibrium point; hence, the system eventually enters a state where the weakened anomaly permits the thermal torque to control the acceleration, and thus to generate a counterclockwise flow. As the anomaly swings back, it comes under the influence of increasingly convergent flow and grows in amplitude. This oscillation is self-sustaining in the proper parameter regime. We also mention that Welander (1986) found self-sustaining saline limit cycles in his relaxation-based loop oscillator.

A further reduction in diffusion apparently permits the salinity anomaly to intensify beyond a critical value, and associated with this is a loss of the oscillation. The new steady equilibrium resembles a relatively sharp saline blob near the bottom of the loop; we shall discuss this limit more quantitatively in a moment.

4.4. *Limit-cycle instability*

A final interesting aspect of the saline limit cycles is that they become unstable. Again, this is a feature that we have discovered numerically and that is dramatically different from the above transitions between steady saline modes and saline limit cycles. Those transitions appeared for varying μ (recall that the limit cycles occurred for a given range of diffusion), while we now focus on a phenomenon occurring for constant μ. We discuss a case for $\lambda/\kappa_S \ll 1$ and $\mu > 1$ (so both thermal and saline modes exist) and for which a saline limit cycle also exists. What we have found is that reductions of α (friction) destabilize the limit cycle such that the system spontaneously transitions to the thermal direct mode. This occurs because a reduction in friction allows faster circulation. The salinity anomaly, when weakened under the precipitation, is then less able to regain its amplitude. In contrast, the rapid relaxation of temperature always ensures the existence of a maximum buoyant temperature torque. Our calculations show that in the proper parameter regime, the system reverts to the thermal mode. There is no analogue of this instability in the box model; as discussed by Stommel, his saline modes are always stable. The only possible mode of state flipping which could be parametrically forced involved a transient frictional increase, thus initiating a flip from a thermal to a saline mode. Here, we emphasize that a decrease in friction can initiate a transition to a thermal mode. The dependence of this instability on the system parameters is complicated, however, and we do not have a complete understanding of it.

4.5. *The weakly diffusive limit*

The analysis presented earlier applied for small λ/κ_S. The previous numerically generated steady states were all consistent with this constraint and yielded results in agreement with the predictions. It remains to examine the solutions for which λ/κ_S is not small, a limit not as readily amenable to analysis but easily handled numerically.

The parameter μ tends to be large for λ/κ_S not small; our previous analysis suggests that both saline and thermally direct cells should exist. Our numerical experimentation has confirmed this. The quantitative details of the thermally direct modes in this limit

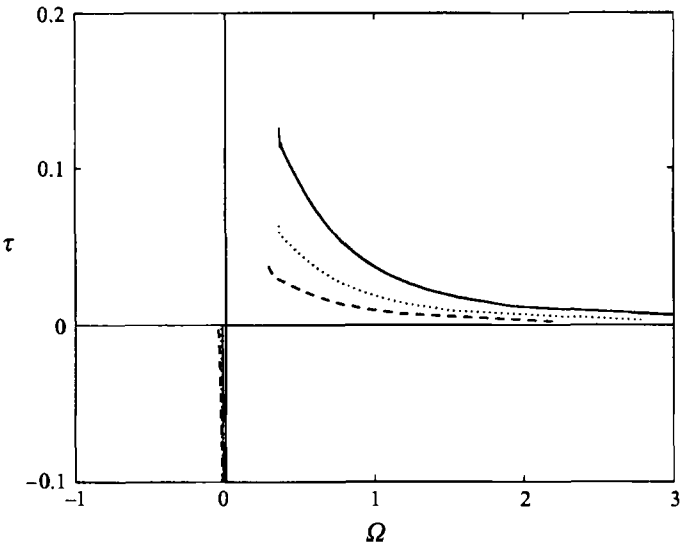

FIGURE 16. Numerical solutions for $\lambda/\kappa_S = 1$. The same convention as figure 13 is used. A naive application of the strongly diffusive solution works well for the thermal modes, but fails for the saline modes. $\lambda = \kappa_S = \kappa_T = 0.015$, and $\gamma = 0.5$.

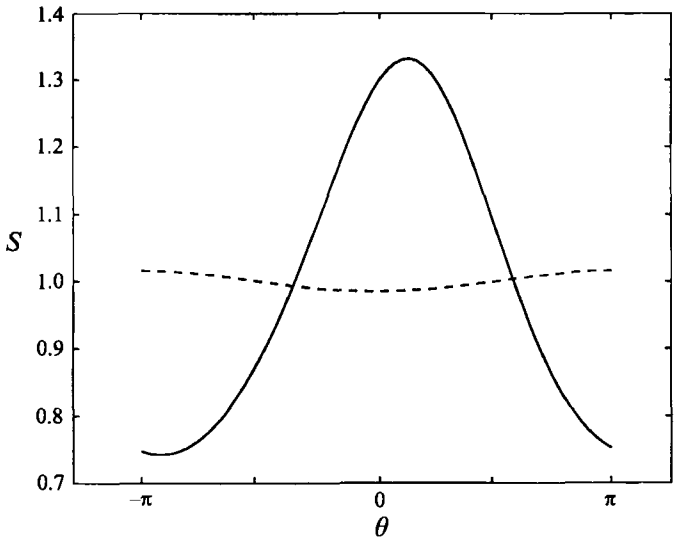

FIGURE 17. Salt profiles for $\lambda/\kappa_S = 1$, and $\lambda = \kappa_S = \kappa_T = 0.015$, $\alpha = 0.01$, $R = 5.6$, and $\gamma = 0.5$: azimuthal angle from $-\pi$ to π versus salinity amplitude. The dashed line is from a thermally direct mode and the solid line is from a saline mode. Note in the latter the appearance of an isolated salinity maximum for small positive angles, while the remainder of the loop is relatively fresh.

are also explained well by the earlier solution. This is illustrated in figure 16, which displays the numerically determined phase-space behaviour of the loop oscillator for λ/κ_S not small. These experiments employ $\lambda = \kappa_S = \kappa_T = 0.015$, (i.e. $\lambda/\kappa_S = 1.0$), and $\gamma = 0.5$. The three employed R-values correspond to those in the earlier small λ/κ_S experiments, and yield μ-values of roughly 11, 5.6 and 2.8.

The saline modes are, however, not well predicted quantitatively by (4.8). Examples of salinity structure for both the thermal and saline modes appear in figure 17, which

also suggests why the small-λ/κ_S solution quantitatively fails for the saline mode. The salinity profile consists of relatively fresh water with a mass of highly salty water located near the loop bottom (i.e. near $\theta = 0$). Note that the maximum salinity value is roughly 1.35 and the minimum is roughly 0.75. Thus, the salinity distribution is not symmetric in extreme values. Such structure cannot be well approximated by $\sin\theta$ and $\cos\theta$ terms only, which in turn represent the lowest-order terms of the Taylor expansion for the exponential functions in the exact salinity solution (see (4.6)).

To understand the physical reasons for the appearance of this structure, it is again useful to recall the results of §3. The 'salt-spike' solutions there arose because the plugs spent most of their time under the regions of evaporation, and hence were intensified by the associated convergence. Similar dynamics apply here; their relevance can be demonstrated by following the procedure used earlier. Namely, diffusion is neglected entirely and we assert

$$S = 2\pi\delta(\theta - \theta_0) \tag{4.14}$$

as an ansatz. The factor 2π appears from normalization and δ represents the usual Dirac delta function. Thus we search for salinity solutions concentrated at angle θ_0 within the loop, and propose to calculate θ_0.

Inserting (4.14) in (2.12*a*) with $\kappa_S = 0$, multiplying by any non-trivial periodic function and averaging over the loop yields

$$\Omega = -\lambda\cos\theta_0. \tag{4.15}$$

Assuming $\kappa_T = 0$ and a weak Ω (the latter an unnecessary mathematical simplification) yields

$$T = \Delta\sin\theta \tag{4.16}$$

as the leading-order temperature solution. The momentum equation (2.12*c*) thus becomes

$$\sin\theta_0 - \alpha\lambda\cos\theta_0 = \Delta/2R, \tag{4.17}$$

which, given that α and λ are small, has the solution

$$\sin\theta_0 \approx \Delta/2R > 0 \tag{4.18}$$

to a high degree of accuracy. For small θ_0, (4.15) gives

$$\Omega \approx -\lambda. \tag{4.19}$$

It is interesting that we have found numerical support for these formulae, particularly for (4.19). Equation (4.18) is also consistent with the structure in figure 17. The solution there consists of a salinity maximum off-centred from the bottom slightly in the counter-clockwise direction. This in turn provides just enough salinity torque to almost cancel the temperature torque (note that friction is unimportant in the solution). Some overturning is still required to maintain the salinity anomaly off-centre, thereby providing a torque. Equation (4.19) demonstrates this velocity is $O(\lambda)$ in magnitude, and is just sufficient to keep the salinity blob under the evaporation. The utility of these solutions is all the more surprising given that the ansatz in (4.14) is not a particularly good approximation of the salinity structure. Nonetheless, the comparisons argue that the solution in figure 17 is related to the salt-spike solutions of §3. Its appearance accounts for the quantitative mismatch between the earlier analytical solution and the present numerical results. (A further discussion of the inaccuracy of the Ω predictions from the $\lambda/\kappa_S \ll 1$ theory appears below.) Its physical interpretation is of a system with weak enough mixing that all the heavy salt mass is trapped at the vessel bottom. No analogue of this structure appears in the box model.

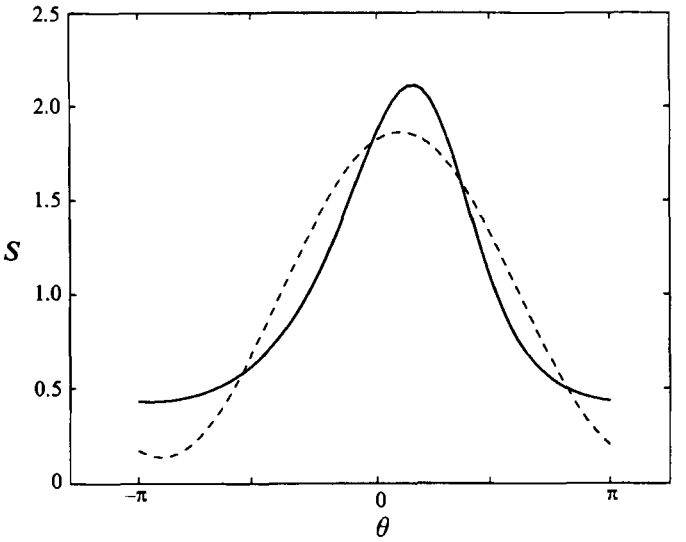

FIGURE 18. A comparison of salinity profiles for $\lambda/\kappa_S = 3$. The solid curve comes from an experiment using natural boundary conditions and the dashed curve from one with virtual salt flux. The parameters are $\lambda = 0.015$, $\kappa_S = \kappa_T = 0.005$, $\gamma = 0.5$ and $R = 0.5$. There is a coarse scale agreement between the profiles, but the salinity magnitudes and structure quantitatively disagree.

4.6. *Virtual salt flux boundary conditions*

We have also examined loop oscillator behaviour subject to the so-called virtual salt flux boundary condition (VSF) to learn about relevant dependencies of the solutions. It is a simple matter to show in this case that (2.12) become

$$S_t + \Omega S_\theta = \lambda \sin\theta + \kappa_S S_{\theta\theta}, \tag{4.20}$$

$$T_t + \Omega T_\theta = -\gamma(T - \Delta \sin\theta) + \kappa_T T_{\theta\theta}, \tag{4.21}$$

while (2.12*c*) is unchanged. (Note that $\bar{S} = 1$ has been used in (4.20).) The exact steady solutions of (4.20) and (4.21) are

$$T = \frac{\Delta\gamma(\gamma+\kappa_T)\sin\theta - \gamma\Delta\Omega\cos\theta}{\Omega^2 + (\gamma+\kappa_T)^2}, \tag{4.22}$$

$$S = 1 - \frac{\kappa_S\lambda}{\Omega^2+\kappa_S^2}\sin\theta + \frac{\Omega\lambda}{\Omega^2+\kappa_S^2}\cos\theta. \tag{4.23}$$

Thus

$$\alpha\Omega = \frac{-\kappa_S\lambda}{2(\Omega^2+\kappa_S^2)} + \frac{\gamma(\gamma+\kappa_T)\Delta}{2R(\Omega^2+(\gamma+\kappa_T)^2)}, \tag{4.24}$$

which is identical to (4.8). Virtual salt flux conditions thus yield generally the same thermal mode behaviour as do freshwater flux conditions. This is perhaps not surprising as salinity plays a minor role in the thermal mode.

The difference between NBC and VSF condition behaviour hence occurs for saline modes and the differences here are mainly quantitative. Among the interesting saline mode behaviours are the limit-cycle development and the limit-cycle instability. Analogues of all these have been found using VSF. On the other hand, the details of where in parameter space these behaviours set in, and the system values, can differ from those computed using the NBC. One example is to be found in the limit cycles

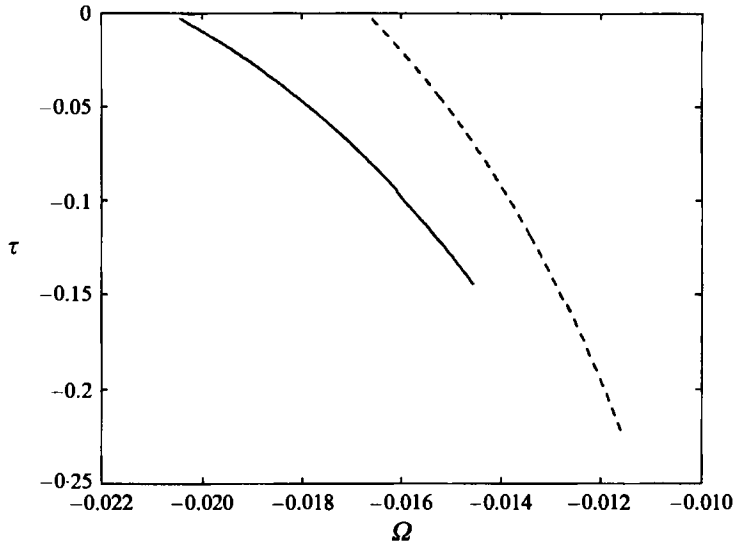

FIGURE 19. The sensitivity of Ω to boundary conditions: virtual (dashed curve) and natural (solid curve) boundary conditions were used in these experiments. $\lambda = 0.015$, $\kappa_S = \kappa_T = 0.005$, $\gamma = 0.5$, and $R = 0.5$. The virtual salt flux experiment consistently returns overturning rates smaller than the natural boundary condition experiment.

appearing in figure 15. The smaller of the two limit cycles was computed using the NBC and the larger using VSF. There is clearly a significant difference in the amplitude of the oscillation as well as in the overturning rates. A second difference is illustrated in figure 18, where salinity profiles appropriate to the parameters $\lambda = 0.015$, $\kappa_S = \kappa_T = 0.005$, and $\gamma = 0.5$ are shown. Note that the structure and amplitude of the salinity profile differs. These can be partially accounted for because VSF constrains the shape of the salinity profile. The amplitude differences also occur because the usual implementation of VSF employs a globally averaged salinity value in specifying the flux. (In this way the phenomena of the salt explosion are avoided.) This constraint has the effect of underestimating the actual flux for high salinity values and overestimating it for low values.

Finally, we demonstrate the sensitivity of the overturning rate to the applied boundary conditions in figure 19, where we compare the phase-space plots for the loop oscillator. The convention in this plot is the same as in several previous ones, with the main difference being that we focus on saline modes only. The parameters for this set of experiments are $\lambda = 0.015$, $\kappa_S = \kappa_T = 0.005$, $\gamma = 0.5$ and $R = 0.5$. The VSF overturning rates are consistently more sluggish than the NBC rates. This reflects the 'broader' salinity profile of the VSF experiments (see figure 18). As a result of being spread out, the salinity torque is weakened in magnitude and drives a slower overturning.

A last point here is that the VSF system yields an overturning formula identical to that of the small-λ/κ_S limit. The relative comparison in figure 19 thus gives an indication of the errors inherent in the application of (4.8) to saline modes for λ/κ_S not small.

5. Discussion

The preceding analysis has explored the haline and thermohaline convective behaviour of a simple yet non-trivial model, i.e. the loop model. This study is meant to complement and extend the enormously useful and more traditional box model studies by graduating to the next level of sophistication, while retaining tractability. One of the main advantages here is that diffusion can be explicitly included. Box models, by their construction, cannot completely include such effects. We have also employed a more accurate representation of surface exchange physics by explicitly including freshwater flux, rather than virtual salt flux. Indeed, a complementary aim of this analysis was to examine a haline buoyancy-driven system of sufficient simplicity that we could isolate its dependence on freshwater flux. Comparison of solutions consistent with both boundary conditions has allowed us to assess their impact on system behaviour.

Freshwater flux is capable of driving haline oscillations in the loop model, although the picture is somewhat modified from that of GCMs. As opposed to virtual salt flux, which leads directly to local salinity modifications, salinity concentrations subject to natural boundary conditions arise because of the secondary velocities directly related to evaporation and precipitation. These in turn lead to buoyancy distributions which drive the loop circulation and provide a feedback which intensifies the anomalies. In a sense, it is the nature of this nonlinear model to establish a coherence between salty waters and regions of evaporation (clearly this feedback appears in the salt equation). This coherence leads to our most dramatic result, i.e. the formation of spikes. We mention this because the above coherence is often recognized as the cause of the so-called salt explosion in models with 'modified' virtual salt flux boundary conditions (i.e. S appears rather than $\bar{S}$). Here the natural boundary condition generates a dramatic increase in salinity magnitude, but it remains bounded and the growth leads to interesting physical behaviour.

It is also appropriate to comment on the evolution of perturbations subject to the natural boundary condition. First, perturbations are advected by the mean flow. Secondly, the stability of the perturbations is independent of the strength of the boundary forcing. In fact, such behaviour is quite consistent with the physical idea that salinity anomalies do not induce a negative feedback to facilitate their removal, as do thermal anomalies. Rather, we find that the decay timescales depend entirely on the internal system parameters, namely diffusion and viscosity. These generally are relatively weak and generate decay timescales long compared to the relaxation times employed in most models. Thus, salinity anomalies are carried by currents where they are formed, and they can travel to quite remote places. We speculate that this is related to the persistence of salinity anomalies (such as the North Atlantic Great Fresh Event of the 1970s) in the open ocean.

A great deal of similarity has also been found between the loop oscillator and box model behaviours, which has aided us in our analysis. This comparison has allowed us to compute certain of the box model parameters from first principles. An example is R, the box model density ratio. We find the effective density ratio, μ, of the loop model to be a function of forcing, relaxation and diffusion, and to play a central role in determining the existence and type of multiple equilibria. Thus, we find a dynamically significant role for diffusion in the loop model, as opposed to the somewhat more passive role it obtains in box models (Thual & McWilliams 1992). An unexpected result is that μ is not unambiguously greater than unity, a result which opens the possibilities of multiple thermally direct cells. A second example is the identification of relaxation

timescale ratios with our parameter $d = \kappa_S/(\gamma+\kappa_T)$. Here a value for this ratio less than 1, as typically assumed, is on much firmer footing. It is nonetheless surprising that this ratio is entirely devoid of the freshwater flux physics driving salinity variations.

As a final point, it is useful to point out the unique dependence of the system behaviour on the various boundary specifications. Not surprisingly, the relaxation condition departs most dramatically from the natural boundary condition in behaviour. It does not create spikes, its timescales differ quantitatively and the details of its steady solutions are also qualitatively different. Virtual salt flux (based on average salinity) tends to mirror the natural boundary condition reasonably well in some parameter regimes. It inaccurately captures the physics leading to limit-cycle behaviour, however, and therefore does not perform well with regard to haline oscillations. It also tends to give an uncontrollable production of negative salinities. This is associated with inaccuracies of the specification of salt flux arising from the use of an averaged salinity in the boundary condition. We do find quantitative support for the use of the virtual salt flux condition when studying thermally direct modes, for the reason that salinity plays a minor role in such solutions. The same cannot be said for saline modes, however. In certain parameter regimes, namely weak freshwater flux–strong diffusion, the steady saline mode solutions are well predicted using virtual salt flux. The characteristics of the saline limit cycle and its stability are, however, sensitive to the employed boundary condition, as are the salinity profiles and the overturning rates in the weakly diffusive limit.

Evidence for saline mode circulations is to be found in paleoclimatic data and has motivated interest in the study of saline modes. Our results suggest that freshwater flux boundary conditions are preferable for this task in order to better ensure accurate modelling of mean structure, overturning and transients. A practical concern relevant to human impact on climate involves the stability of the modern thermal mode thermohaline circulation. Such interest is implicit in the transition studies conducted by, for example, Nakamura, Stone & Marotzke (1994). Given the sensitivity of GCMs to minor variations of their parameters, a premium should be placed on accuracy in modelling the details of the system. The accurate modelling of saline mode dynamics would thus seem to be advisable even in models of present day climate and our results emphasize a central role for the natural boundary condition in achieving this goal.

W. K. Dewar is supported by the NSF through grant OCE-9012114, ONR contract N00014-89-J-1577 and NASA through grant NAGW-3087. R. X. Huang is supported through the NOAA grant NA36GP0270 and through NSF grant OCE93-00706. Sheila Heseltine prepared the manuscript and J. Park assisted with computational aspects of the problem. The authors would particularly like to acknowledge Drs Michael Ghil and James McWilliams, who organized the Climate Systems Modeling Project workshop held in Los Angeles, October 1993. This work was initiated during discussions between the authors at that meeting. Contribution No. 8711 from the Woods Hole Oceanographic Institution.

Appendix A. An analysis of virtual salt flux conditions

The equations are

$$S_t + \Omega S_\theta = -\lambda\cos\theta + \kappa S_{\theta\theta}, \quad \Omega_t = -\alpha\Omega - \langle S\sin\theta\rangle. \qquad \text{(A 1}a, b\text{)}$$

The solution form $S = 1 + a(t)\cos(\theta) + b(t)\sin\theta$ exactly transforms the above into three coupled ordinary differential equations:

$$a_t + \Omega b = -\lambda - a\kappa, \quad b_t - \Omega a = -b\kappa, \quad \Omega_t = -\alpha\Omega - \tfrac{1}{2}b. \qquad \text{(A 2}a\text{–}c\text{)}$$

Higher modes, which may appear because of initial conditions, can be shown to decay exponentially with a timescale proportional to κ^{-1}. Now consider $\alpha \sim \lambda \sim \kappa \ll 1$ and expand (A 2) in λ. At lowest order

$$a_{0_t} - \Omega_0 b_0 = 0, \quad b_{0_t} + \Omega_0 a_0 = 0, \quad \Omega_{0_t} = -\tfrac{1}{2} b_0, \tag{A 3a–c}$$

which after some manipulation yield

$$\dot{\theta}_0^2 = \tfrac{1}{2} r_0 \cos\theta_0 + C, \tag{A 4}$$

where r_0 and C are as yet unknown, $\dot{\theta}_0 = \Omega_0$, $a_0 = r_0 \cos\theta_0$ and $b_0 = r_0 \sin\theta_0$. At $O(\lambda)$, we obtain

$$a_{1_t} + \Omega_0 b_1 + \Omega_1 b_0 = -1 - a_0 \hat{\kappa}, \quad b_{1_t} - \Omega_0 a_1 - \Omega_1 a_0 = -b_0 \hat{\kappa}, \quad \Omega_{1_t} + \tfrac{1}{2} b_1 = -\hat{\alpha}\Omega_0, \tag{A 5a–c}$$

where $\hat{\alpha} = \alpha/\lambda$ and $\hat{\kappa} = \kappa/\lambda$. It is a simple matter to show that the vectors $(a_1, b_1, \Omega_1) = (a_0, b_0, 0)$ and $(-\frac{1}{2}, 0, \Omega_0)$ solve the adjoint operator of the left-hand sides of (A 5). We thus obtain two solvability conditions for purely periodic solutions, i.e.

$$0 = -\int_0^T a_0 \, \mathrm{d}t - r_0^2 T\hat{\kappa}, \quad 0 = -\hat{\kappa}\int_0^T a_0 \, \mathrm{d}t - T - 2\hat{\alpha}\int_0^T \dot{\theta}_0^2 \, \mathrm{d}t, \tag{A 6a, b}$$

which relate the unknown r_0 and C to the system parameters $\hat{\alpha}$ and $\hat{\kappa}$.

Appendix B. A freshwater flux version of Stommel's (1961) box model

B. 1. *The equivalent formula for the Ω-equation*

According to Huang *et al.* (1992), the steady temperature solution for the box model is

$$T = (1+p)\alpha T_0/(1+2c|T-S|); \tag{B 1}$$

the salinity solution is

$$S = p\beta S_0/(|f|), \tag{B 2}$$

where $T = \alpha T_0(T_1 - T_2)$ and $S = \beta S_0(S_1 - S_2)$, p is the precipitation rate, and the overturning rate f is linearly proportional to the density difference $f = c(T-S)$. Introducing $\Omega = 2f$, we have an equation equivalent to the Ω-equation (4.1):

$$\frac{\Omega}{2c\alpha R T_0} = \frac{1+p}{(1+|\Omega|)R} - \frac{2p}{|\Omega|}. \tag{B 3}$$

In the case of virtual salt flux formulation, the first term on the right-hand side is replaced by $1/[(1+|\Omega|)R]$.

B. 2. *The lower limit of the saline mode*

In a saline mode the density gradient due to salinity must be larger than that due to the temperature. Note that in a very slow saline mode, temperature is largely set by the reference temperature, and the upper bound of the salinity difference is just twice the mean salinity; thus, we have

$$\alpha T_0 < \beta(S_1 - S_2) \leqslant 2\beta S_0, \tag{B 4}$$

which is equivalent to a lower limit in R for the saline mode:

$$R \geqslant 1/2. \tag{B 5}$$

In addition, Huang *et al.* (1992) point out that there is a 'forbidden' regime, in which

both interbox exchange rates are equatorward, i.e. pointed away from the region of excess precipitation. The corresponding state is the trivial solution given by

$$T_1 = T_0, \quad T_2 = 0, \quad S_1 = 2S_0, \quad S_2 = 0.$$

Accordingly, the condition defining this regime is

$$|c(T-S)| < p/2, \tag{B 6}$$

or in dimensional units

$$|-\alpha T_0 + \beta(S_1 - S_2)| \leqslant p/2c; \tag{B 7}$$

thus, (B 2) is invalid within this forbidden regime. Because $S_1 - S_2 = 2$ for this special state, the corresponding regime in terms of the density ratio is

$$\frac{1}{2} - \frac{p}{4c\alpha T_0} \leqslant R \leqslant \frac{1}{2} + \frac{p}{4c\alpha T_0}. \tag{B 8}$$

Thus, when $R \leqslant \frac{1}{2} - p/(4c\alpha T_0)$, there is no stable saline solution. Thus the box model based on freshwater flux is similar to the box model based on relaxation conditions. The critical value of R close to $\frac{1}{2}$ in the present case is due to the possibility of all the salt being flushed into the southern box. In the relaxation case, total salt is not conserved, so the maximum salinity difference is just S_0, instead of $2S_0$ as in the case with the natural boundary conditions.

On the other hand, the behaviour of a model based on the virtual salt flux formulation is rather different. There is always a saline mode, no matter how small the density ratio. Of course, such a saline mode may not be a physical solution. As the overturning becomes slower, the salinity difference diverges, and salinity in the northern box can become negative. Such a non-physical result nonetheless represents an acceptable mathematical solution.

B. 3. *The upper limit of the thermal mode*

The non-existence of the thermal mode can be explained as follows. The maximum temperature difference is T_0. Since the salinity torque acts against the thermal torque, the circulation rate satisfies

$$f < c\alpha T_0. \tag{B 9}$$

As a result, the salinity satisfies

$$\beta S = \frac{p\beta S_0}{f} > \frac{p\beta S_0}{c\alpha T_0} = \frac{p}{c} R. \tag{B 10}$$

However, if the density gradient due to this salinity is larger than that due to temperature, i.e.

$$\beta S = \frac{p}{c} R > \alpha T_0 \quad \text{or} \quad \frac{p}{c} > \frac{\alpha T_0}{R}, \tag{B 11}$$

then such a thermal mode is impossible. From the analysis above, it is clear that for a given density ratio R, strong friction (small c) or strong freshwater flux eliminates the thermal mode.

The upper limit of the thermal mode can be estimated more precisely. The critical situation is the case when the straight line, representing frictional torque, just touches the gravitational torque curve in the Ω-diagram, figure 13. Writing the Ω-equation as

$$\lambda f = F(f), \tag{B 12}$$

the location of this point, f_c, is determined by

$$dF(f)/df = F/f. \tag{B 13}$$

For the natural boundary condition model, this leads to

$$4Rp(1+f)^2-(1+p)f(1+2f) = 0, \tag{B 14}$$

with solution

$$f_c = \frac{-(1+p-8Rp)+[(1+p)(1+p+16Rp)]^{1/2}}{4(1+p-2Rp)}. \tag{B 15}$$

Assuming $p \ll 1$, the approximate solution is

$$f_c = 4Rp-(8R^2+6R-0.125)p^2+O(p^3). \tag{B 16}$$

Substituting into (B 12), our estimate of the boundary is

$$p \approx \frac{c\alpha T_0}{4R(1+2c\alpha T_0)}. \tag{B 17}$$

For the case discussed by Huang *et al.* (1992), (B 17) predicts the limit of the thermal mode with an error of less than 5%.

REFERENCES

Broecker, W. S., Bond, G., Klas, M., Bonani, G. & Wolfli, W. 1990 A salt oscillator in the glacial Atlantic? 1. The concept. *Paleoceanography* **5**, 469–477.

Broecker, W. S., Peteet, D. M. & Rind, D. 1985 Does the ocean-atmosphere system have more than one stable mode of operation? *Nature* **315**, 21–25.

Bryan, F. 1986 High-latitude salinity effects and interhemispheric thermohaline circulations. *Nature* **323**, 301–304.

England, M. H. 1993 Representing the global-scale water masses in ocean general circulation models. *J. Phys. Oceanogr.* **23**, 1523–1552.

Huang, R. X. 1993 Real freshwater flux as a natural boundary condition for the salinity balance and thermohaline circulation forced by evaporation and precipitation. *J. Phys. Oceanogr.* **23**, 2428–2446.

Huang, R. X. & Chou, R. L. 1994 Parameter sensitivity study of the saline circulation. *Climate Dyn.* **9**, 391–409.

Huang, R. X., Luyten, J. R. & Stommel, H. M. 1992 Multiple equilibrium states in combined thermal and saline circulation. *J. Phys. Oceanogr.* **22**, 231–246.

Keller, J. 1966 Periodic oscillations in a model of thermal convection. *J. Fluid Mech.* **26**, 599–606.

Malkus, W. R. 1972 Non-periodic convection at high and low Prandtl number. *Mem. Soc. R. Sci. Liege* (6) **4**, 125–128.

Marotzke, J. 1994 Ocean models in climate problems. In *Ocean Processes in Climate Dynamics: Global and Mediterranean Examples* (ed. P. Malanotte-Rizzoli & A. R. Robinson). NATO ASI Series C, vol. 419, pp. 79–109). Kluwer.

Marotzke, J. & Willebrand, J. 1991 Multiple equilibria of the global thermohaline circulation. *J. Phys. Oceanogr.* **21**, 1372–1385.

Nakamura, M., Stone, P. H. & Marotzke, J. 1994 Destabilization of the thermohaline circulation by atmospheric eddy transports. *J. Climate* **7**, 1870–1882.

Stommel, H. M. 1961 Thermohaline convection with two stable regimes of flow. *Tellus* **13**, 224–230.

Thual, O. & McWilliams, J. C. 1992 The catastrophe structure of thermohaline convection in a two-dimensional fluid model and a comparison with low-order box models. *Geophys. Astrophys. Fluid Dyn.* **64**, 67–95.

TRENBERTH, K. E. & SOLOMON, A. 1994 The global heat balance: heat transports in the atmosphere and the ocean. *Climate Dyn.* **10**, 107–134.

WALIN, G. 1985 The thermohaline circulation and the control of ice ages. *Palaogeogr., Palaeoclimatol., Palaeoecol.* **50**, 323–332.

WANG, Y. Z. & BAU, H. H. 1992 Thermal convection loop with heating from above. *Intl J. Heat Mass Transfer* **35**, 111–120.

WEAVER, A. J. & SARACHIK, E. S. 1991 The role of mixed boundary conditions in numerical models of the ocean's climate. *J. Phys. Oceanogr.* **21**, 1470–1493.

WELANDER, P. 1967 On the oscillatory instability of a differentially heated fluid loop. *J. Fluid Mech.* **29**, 17–30.

WELANDER, P. 1986 Thermohaline effects in the ocean circulation and related simple models. In *Large-Scale Transport Processes in Oceans and Atmospheres* (ed. J. Willebrand & D. L. T. Anderson). NATO ASI Series C: vol. 190, pp. 163–200.

WINTON, M. & SARACHIK, E. S. 1993 Thermohaline oscillations induced by strong steady salinity forcing of ocean general circulation models. *J. Phys. Oceanogr.* **23**, 1389–1410.